Kevin S. Olsen[1,2], Anna A. Fedorova[3], David M. Kass[4], Armin Kleinböhl[4], Alexander Trokhimovskiy[3], Oleg I Korablev[3], Franck Montmessin[5], Franck Lefèvre[5], Lucio Baggio[5], Juan Alday[2], Denis A. Belyaev[3], James A. Holmes[2], Jonathon P. Mason[2], Paul M. Streeter[2], Kylash Rajendran[2], Manish R Patel[2], Andrey Patrakeev[3], and Alexey Shakun[3]

[1]Department of Physics, University of Oxford, Oxford, UK.
[2]School of Physical Sciences, The Open University, Milton Keynes, UK.
[3]Space Research Institute (IKI), Moscow, Russia.
[4]Jet Propulsion Laboratory (JPL), California Institute of Technology, Pasadena, USA.
[5]Laboratoire Atmosphères, Milieux, Observations Spatiales (LATMOS/CNRS), Paris, France.

March 22, 2024

Relationships between HCl, H2O, aerosols, and temperature in the Martian atmosphere Part I: climatological outlook

Kevin S. Olsen[1,2], Anna A. Fedorova[3], David M. Kass[4], Armin Kleinböhl[4], Alexander Trokhimovskiy[3], Oleg I Korablev[3], Franck Montmessin[5], Franck Lefèvre[5], Lucio Baggio[5], Juan Alday[2], Denis A. Belyaev[3], James A. Holmes[2], Jonathon P. Mason[2], Paul M. Streeter[2], Kylash Rajendran[2], Manish R Patel[2], Andrey Patrakeev[3], and Alexey Shakun[3]

[1]Department of Physics, University of Oxford, Oxford, UK.
[2]School of Physical Sciences, The Open University, Milton Keynes, UK.
[3]Space Research Institute (IKI), Moscow, Russia.
[4]Jet Propulsion Laboratory (JPL), California Institute of Technology, Pasadena, USA.
[5]Laboratoire Atmosphères, Milieux, Observations Spatiales (LATMOS/CNRS), Paris, France.

March 05, 2024

Abstract

Detecting trace gases such as hydrogen chloride (HCl) in Mars' atmosphere is among the primary objectives of the ExoMars Trace Gas Orbiter (TGO) mission. Terrestrially, HCl is closely associated with active volcanic activity, so its detection on Mars was expected to point to some form of active magmatism/outgassing. However, after its discovery using the mid-infrared channel of the TGO Atmospheric Chemistry Suite (ACS MIR), a clear seasonality was observed, beginning with a sudden increase in HCl abundance from below detection limits to 1-3 ppbv in both hemispheres coincident with the start of dust activity, followed by very sudden and rapid loss at the southern autumnal equinox. In this study, we have investigated the relationship between HCl and atmospheric dust by making comparisons in the vertical distribution of gases measured with ACS and aerosols measured co-located with the Mars Climate Sounder (MCS). This study includes HCl, water vapour, and ozone measured using ACS MIR, water vapour and temperature measured with the near infrared channel of ACS, and temperature, dust opacity, and water ice opacity measured with MCS. In Part I, we present the methods, observations of HCl, and describe the seasonal evolution of the vertical structure of each of these above quantities. The studied time period encompasses solar longitude 180°-360° in Mars years 34-36, covering the dusty period around perihelion. In Part II, we investigate the quantitative correlations between each quantity and discuss the possible source and sinks of HCl, their likelihood given the correlations, and any issues arising from them.

Plain Language Summary

After four full Martian years in orbit since 2018, the ExoMars Trace Gas Orbiter (TGO) has observed three Martian dusty seasons, which occur when it is spring and summer in the southern hemisphere. The first, starting in summer 2018, featured a global dust storm (GDS) after which we made the first detection of hydrogen chloride (HCl) in the Martian atmosphere using the Atmospheric Chemistry Suite (ACS) instrument. Finding this gas was a priority of ExoMars because its presence hints at the planet being volcanically active. Since then, we have observed two more dusty periods without a GDS and observed the reappearance of HCl each time. Here, we present the climatology of HCl in both hemispheres over these three dusty periods (in Mars years 34, 35, and 36) and investigate their relationships with temperature and water vapour measured by ACS, and with airborne dust and water ice measured with the Mars Climate Sounder (MCS) on the Mars Reconnaissance Orbiter (MRO). In this paper, Part I, we take a qualitative look at how the vertical structure of each quantity changes over time.

1 Introduction

Chlorine plays a major role in the Earth's atmosphere, cycling between the biosphere, lithosphere, hydrosphere, and atmosphere. In Earth's troposphere, it is closely related to evaporation of sea water and the acidification of rain. In the stratosphere, which is much more similar to the lower atmosphere of Mars in terms of pressure and density, it is closely related to ozone chemistry, participating in catalytic cycles of ozone loss. Aside from sea-salt aerosols and anthropomorphic emissions in the troposphere, the next largest natural source of HCl in Earth's atmosphere is volcanic emissions, which are highly variable (Graedel & Keene, 1995; Keene et al., 1999). The largest mechanisms for the removal of reactive chlorine species on Earth is deposition with rain and reaction with hydrocarbons, especially methane (CH_4), and ozone (O_3) (von Glasow & Crutzen, 2003; Wang et al., 2019).

The presence of Hydrogen chloride (HCl) in the atmosphere of Mars may be an indicator for active geological processes such as volcanism or magmatic processes (Wong et al., 2003; Hartogh et al., 2010). For this reason, the presence of HCl on Mars was long searched for, setting stringent upper limits of 0.2 to 0.3 parts per billion by volume (ppbv) (Krasnopolsky et al., 1997; Hartogh et al., 2010; Villanueva et al., 2013). HCl was recently discovered in the lower atmosphere of Mars using the mid-infrared channel of the Atmospheric Chemistry Suite (ACS MIR) onboard the ExoMars Trace Gas Orbiter (TGO) (Korablev et al., 2021), accomplishing one of the primary objectives of the TGO mission - to detect novel trace gases that may be diagnostic of active geological, or biological, processes. ACS MIR measurements determined volume mixing ratios (VMRs) an order of magnitude higher than previous detection limits, but with strong seasonal cycles - seasons that were not probed in past observation attempts.

ACS MIR began its nominal science phase in April 2018, at Martian solar longitude (L_s) 163° in Mars year (MY) 34. Seasonal dust activity began shortly after the southern vernal equinox at $L_s = 180°$ and developed into the 2018 global dust storm (GDS) (e.g. (Kass et al., 2019; Smith, 2019)). Once the GDS subsided, which severely limited the lower reach of ACS MIR solar occultation measurements in the Martian atmosphere, the spectral signature of HCl became prominent in ACS MIR spectra through to the end of the Martian year (Korablev et al., 2021). Outside the Martian dusty season, when Mars approaches aphelion, HCl was only detected twice at high northern latitudes (Olsen et al., 2021). Over the following perihelion periods in MYs 35 and 36, when it is spring and summer in the southern hemisphere, HCl reappeared again, suggesting that its sources and sinks are strongly associated with the seasonal changes in airborne dust loading, water vapour, and atmospheric temperature.

Here, we present the climatology of Martian HCl from three full Martian dusty seasons. HCl abundances are compared to simultaneous measurements of water vapour and temperature, and coincident measurements of the opacities of dust and water ice measured by the Mars Climate Sounder (MCS) (McCleese et al., 2007) on the Mars Reconnaissance Orbiter (MRO) (Zurek & Smrekar, 2007). This study is divided into two parts; this manuscript, Part I, details the methods by which trace gas abundances are measured with ACS MIR, how co-located measurements made with ACS NIR and MCS are determined and compared, what the climatological evolution of each quantity is, and how each quantity is related to one another. In Part II (Olsen et al., 2024), we present a quantitive comparison between each quantity, investigate their correlations, and discuss the possible sources and sinks of atmospheric chlorine on Mars in the context of our observations.

2 Methods

ACS MIR is a cross-dispersion spectrometer operating in solar occultation geometry on the TGO spacecraft, which orbits Mars with an inclination of 74° and a near-circular orbit of 400 km. Solar occultation opportunities arise twice per 2 hour orbit and the spacecraft pointing is shared between ACS and the solar occultation channel of the NOMAD instrument (Nadir and Occultation for Mars Discovery). Occultation opportunities dedicated to ACS MIR measurements are further divided among the configuration of its crossdispersion gratings.

The ACS MIR instrument consists of foreoptics, collimating mirrors, a primary echelle grating that provides access to the mid-infrared spectral range, a secondary collimater, a steerable diffraction grating that separates the overlapping diffraction orders, and a detector (Korablev et al., 2018). The angle of the secondary grating determines which diffraction orders are measured, and the total instantaneous spectral range. HCl lines are present from across the diffraction band centered around 2890 cm^{-1}. These HCl lines are present in secondary grating positions 11 and 12 which cover the spectral ranges 2678-2948 cm^{-1} (diffraction orders 160-175) and 2917-3235 cm^{-1} (orders 173-192), respectively. Each HCl line features a pair of two isotopologues, with the primary, $H^{35}Cl$, being accompanied by a secondary, $H^{37}Cl$. This allows the measurement of their ratio (Trokhimovskiy et al., 2021; Liuzzi et al., 2021). Between the start of the mission and the end of MY 36, ACS MIR has recorded 1127 occultation sequences with position 11 and 1167 with position 12.

Spectra are recorded on a two dimensional detector array over which the x-axis corresponds to wavenumber and the y-axis corresponds to both the diffraction order and the vertical field-of-view (FOV) of the instrument. The raw data appear as several horizontal brightness stripes, where each stripe is a unique diffraction order, the width of each stripe represents the instantaneous FOV, and dark regions separating the stripes are due to portions of the optics not illuminated by the solar disk. Examples of raw data frames are given in (Trokhimovskiy et al., 2020) and (Olsen et al., 2021).

From a single data frame, 10-12 rows can be extracted for each diffraction order, each corresponding to a unique tangent height. In solar occultation mode, a series of observations are made from the surface to above the top of the atmosphere with vertical separations of 1-5 km. Extracted spectra are grouped by their relative positions on the data frame, resulting in 10-12 distinct sequences of occultation spectra for each series of observations made during an occultation opportunity. These are analyzed individually and the weighted means of the retrieved vertical profiles of trace gas volume mixing ratio (VMR) are taken to be the best estimate of the target gas' abundance.

Spectral fitting is performed with the JPL Gas Fitting Software Suite (GGG or GFIT) (Sen et al., 1996; Irion et al., 2002; Wunch et al., 2011) which has been developed for use with ACS MIR (Olsen et al., 2021). A forward model is computed using the HITRAN2020 spectroscopic line list (Gordon et al., 2021) and vertical profiles of temperature and pressure measured simultaneously using the near infrared channel (NIR) of ACS (Fedorova et al., 2023; Fedorova et al., 2020). Where available, broadening parameters for a CO_2-rich atmosphere are used for HCl (Wilzewski et al., 2016) and H_2O/HDO (Gamache et al., 2016; Devi et al., 2017) are used. For occultations where a simultaneous ACS NIR temperature profile was not measured, the temperature and pressure are estimated using the LMD Planetary Climate Model (PCM; (Forget et al., 1999; Lefèvre et al., 2021)) using dust climatologies for each MY from (Montabone et al., 2015; Montabone et al., 2020). Spectral fitting is performed over narrow windows ˜7 cm^{-1} wide using the non-linear Levenberg-Marquardt method. Spectra from each altitude are fitted independently. The matrices of estimated slant column abundances for all observed tangent altitudes and of the calculated slant column paths traced through the atmosphere are inverted using a linear equation solver to obtain a retrieved VMR vertical profile. The resulting VMR vertical profiles are on a 1-km tangent height grid above the Martian areoid.

Retrievals are performed for ten data rows (unique spectra) for each diffraction order at each observed altitude. The retrieved vertical profile is the weighted mean of these ten results, and the uncertainty at each altitude is the standard deviation of the mean. The weights are based on the the uncertainties of the individual retrievals, the diagonal elements of the covariance matrices. Whether HCl or ozone were detected in the ACS MIR spectra was defined as the resulting vertical profiles of VMRs having a 3-σ significance at enough pressure levels on the 1-km retrieval grid to cover the altitude range of two or more solar occultation tangent heights. For very small abundances at the limits of the ACS MIR capabilities, we ensure that a trace gas detection was made in multiple diffraction orders and at multiple tangent heights, as demonstrated in (Korablev et al., 2021). To avoid false-positive results, data above 30 km where the standard deviation of the results from the ten rows is greater than 4 ppbv are rejected, as are sparse vertical profiles where the tangent heights at which HCl was detected are not continuous. Observations where HCl only appears above 30 km, that do not have robust, verifiable absorption lines visible between 10-20 km, are not considered unambiguous detections either. This is based on a careful examination of the fitted absorption features which do not exceed the noise level.

This method has proven to be very effective when examining trace gases in the Martian atmosphere whose absorption features approach the noise levels of the signal. The JPL Gas Fitting Software was originally applied to single spectra to measure carbon monoxide (CO), ozone, and HCl (Olsen et al., 2021; Korablev et al., 2021; Olsen et al., 2020), and the expansion of the method to use multiple detector rows was developed for HCl (Olsen et al., 2021) and then applied to ozone, water vapour, and CO (Olsen et al., 2022; Alday et al., 2023). Example profiles of the VMRs of HCl and H_2O retrieved from the ACS MIR data using these methods are shown in Fig. S1.

3 ACS MIR and MCS Data

The latitudinal distribution of ACS solar occultation observations is shown in Fig. 1 from the start of the primary science phase at $L_s = 163°$ in MY 34 to $L_s = 120°$ MY 37. The latitude of the occultations changes as the orbital plane precesses around Mars and gaps occur when the angle between the Sun and spacecraft's orbital plane (beta) approaches perpendicularity with the Mars-Sun axis. The northern and southern reach is a function of the orbital inclination of Mars and the Martian season. Each solar occultation occurs at the local solar terminator, and so the northernmost or southernmost occultation opportunities occur at the edges of the polar day or polar night. Thus the ACS occultations have the greatest latitudinal extent at the equinoxes.

Perihelion, the closest approach between Mars and the Sun, occurs at $L_s = 251°$ towards the end of southern spring and just before southern summer, while aphelion occurs at $L_s = 71°$ prior to southern winter. Herein we refer to the first half of the Martian year, from the southern autumnal equinox ($L_s = 0°$) to the vernal equinox ($L_s = 180°$), the aphelion period, and the second half of the year as the perihelion period. This is due to the north-south symmetry in the Martian climate exhibited above 5-10 km (Fedorova et al., 2023).

Indicated in Fig. 1 are the locations where HCl or ozone were detected in the ACS MIR observations. Both gases show strong seasonal preference and north-south symmetry which will be discussed in detail in section .

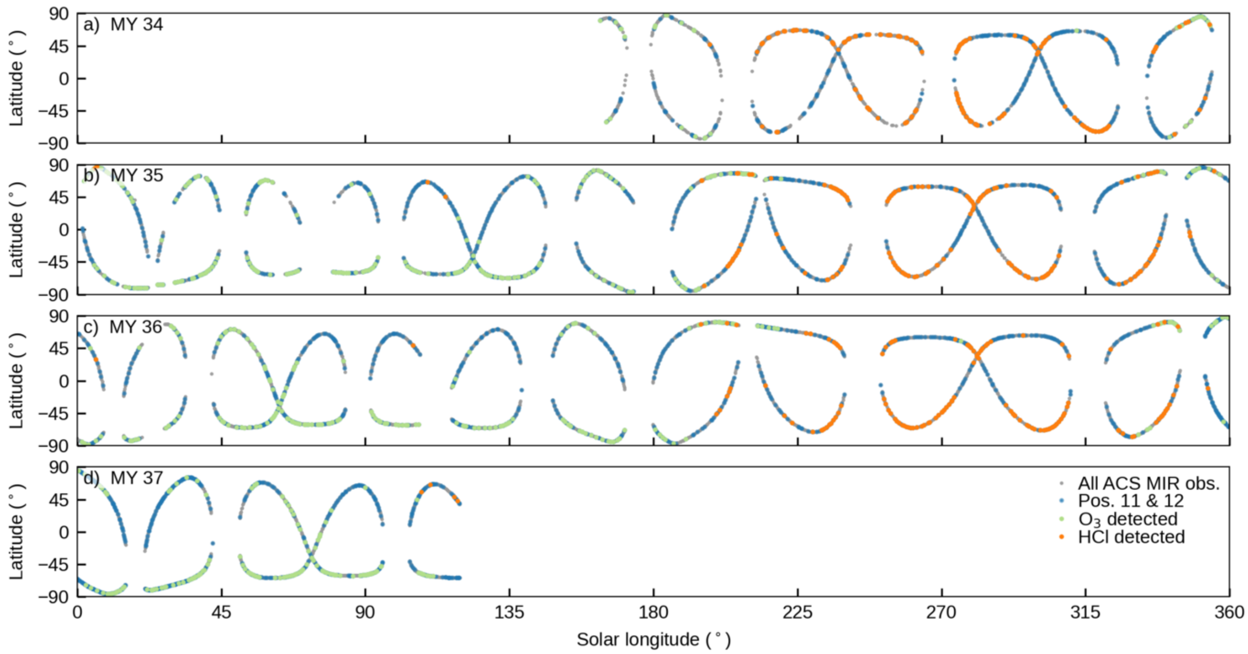

Figure 1: Distribution of ACS MIR solar occultation observations. The data shown are the latitudes of ACS MIR solar occultation observations as a function of time, indicated as solar longitude (L_s) over the year. The panels from top to bottom are for different Mars years (MYs) from the start of ExoMars science operation in MY 34 (a), through MY 37 (d), the current MY at the time of writing. Observations in which ozone was detected are highlighted green, and cover southern fall and winter. Those where HCl was detected are highlighted orange and occur during southern spring and fall.

MCS is a passive radiometer with nine channels that operates in nadir, off-nadir, and limb geometries. The infrared channels cover absorption features of CO_2, used for retrieval of pressure and temperature, as well as absorption features of aerosols, used for retrieval of water ice and dust opacity (McCleese et al., 2007). The dust opacity per km is measured at 21.6 µm and that of water ice is measured at 11.9 µm. The current version of MCS data, v5.2, uses a two-dimensional radiative transfer scheme to correct for lateral gradients in temperatures and aerosols (Kleinböhl et al., 2009; Kleinböhl et al., 2017). For a portion of the MCS data set that covers the MY 34 global dust storm, MCS data was reprocessed using a far infrared channel to improve its vertical range (v5.3.2) (Kleinböhl et al., 2020).

The MRO spacecraft is in a Sun-synchronous orbit (inclination 93°) at an altitude of 250-316 km. MCS nominally operates in limb viewing mode and makes frequent, 30-s observations throughout its orbit, amassing hundreds of measurements per day over a broad range of latitudes and longitudes. This provides ample opportunity to find coincident measurements between ACS MIR solar occultations, and MCS limb scans. MCS observations at mid-to-low latitudes are made at approximately 03:00 and 15:00 local time, but this time can vary within a ˜2 hr window depending on the time of year, especially at higher latitudes, where the majority of ACS solar occultations occur.

The coincidence criteria set to determine an MCS-ACS coincident measurements was within ± 0.125° L_s (˜6 hours) and spatially separated by a distance < 500 km. This results in the MCS observation ground track intercepting a solar occultation location for 85% of the ACS observations, often with around ten MCS limb observations per ACS tangent point. An example of the geometry of a coincident measurement is shown in Fig. 2, which has all MCS and ACS MIR observations made within the coincidence criteria. Example profiles of the measured quantities compared here, the VMRs or HCl and H_2O measured with ACS MIR, temperatures from ACS NIR and MCS, and the opacities of dust and water ice measured with MCS, are shown in Fig. S1.

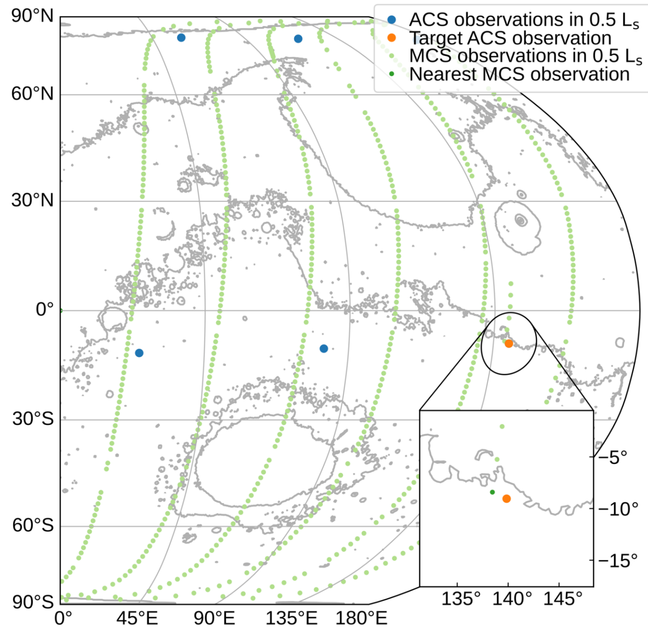

Figure 2: Coincident observations between ACS and MCS. Shown is the eastern hemisphere of Mars with the location of an ACS MIR occultation where HCl was detected and coincident MCS observations were found (orange and inset). An area covering 500 km from the occultation tangent point is indicated. Each MCS observation made within a 0.25° L_s window of the ACS MIR occultation is indicated (green), as are other ACS MIR observations (blue). The inset highlights the ACS MIR occultation, the coincident MCS observations, and the MCS observation nearest in space and time to ACS MIR.

4 Results

4.1 The climatology of HCl observed with ACS MIR

Since HCl was observed for the first time in the Martian atmosphere, we have noted that it is apparently correlated with water vapour and behaves with a linked seasonality (Olsen et al., 2021; Korablev et al., 2021; Aoki et al., 2021). At this time, we have made observations of HCl through three perihelion periods in MYs 34, 35, and 36 and have performed retrievals with both positions 11 and 12. This provides an unprecedented opportunity to explore the repeating seasonal changes in HCl over altitude and over time. In general, the VMR of HCl remains below the limits of a definitive detection during the aphelion periods, which are not shown. That is, HCl may be present at low levels, well below 0.5 ppbv, but the absorption features present in such spectra are not prominent beyond the instrument noise, and a low detection limit is determined rather than an HCl VMR (Olsen et al., 2021).

Immediately following the southern vernal equinox at $L_s = 180°$, HCl becomes detectable and VMRs increase rapidly. HCl then remains in the Martian atmosphere with VMRs of several ppbv throughout the perihelion period. Around the southern autumnal equinox, the HCl VMR falls off dramatically, and remain low through the next aphelion period until it is spring in the southern hemisphere again. Such an overall trend is apparent in both hemispheres, but the magnitudes in the southern hemisphere grow much larger, and vary in a more dynamic fashion, than in the north.

Fig. 3 shows how the vertical distribution of HCl changes with time, as observed with ACS MIR over the perihelion periods. There is a strong similarity in the southern hemisphere evolution each MY, and a striking difference between the abundances in the northern and southern hemispheres. It is important to note that empty space in Fig. 3 does not indicate a lack of HCl, but no observations. Grey shading indicates when secondary grating positions 11 or 12 were used, but HCl remained below a detection threshold. MY 34 was punctuated by the GDS that strongly impeded our ability to probe the lower atmosphere and resulted in the lack of observations between $L_s = 190^{\circ}$ and 240°, especially below 30 km. Other visible gaps in the data set are due to unfavourable beta angles, as shown in Fig. 1. Sections of the latitude coverage shown in Fig. 1 that correspond to each panel in Fig. 3 are reproduced in Fig. S2.

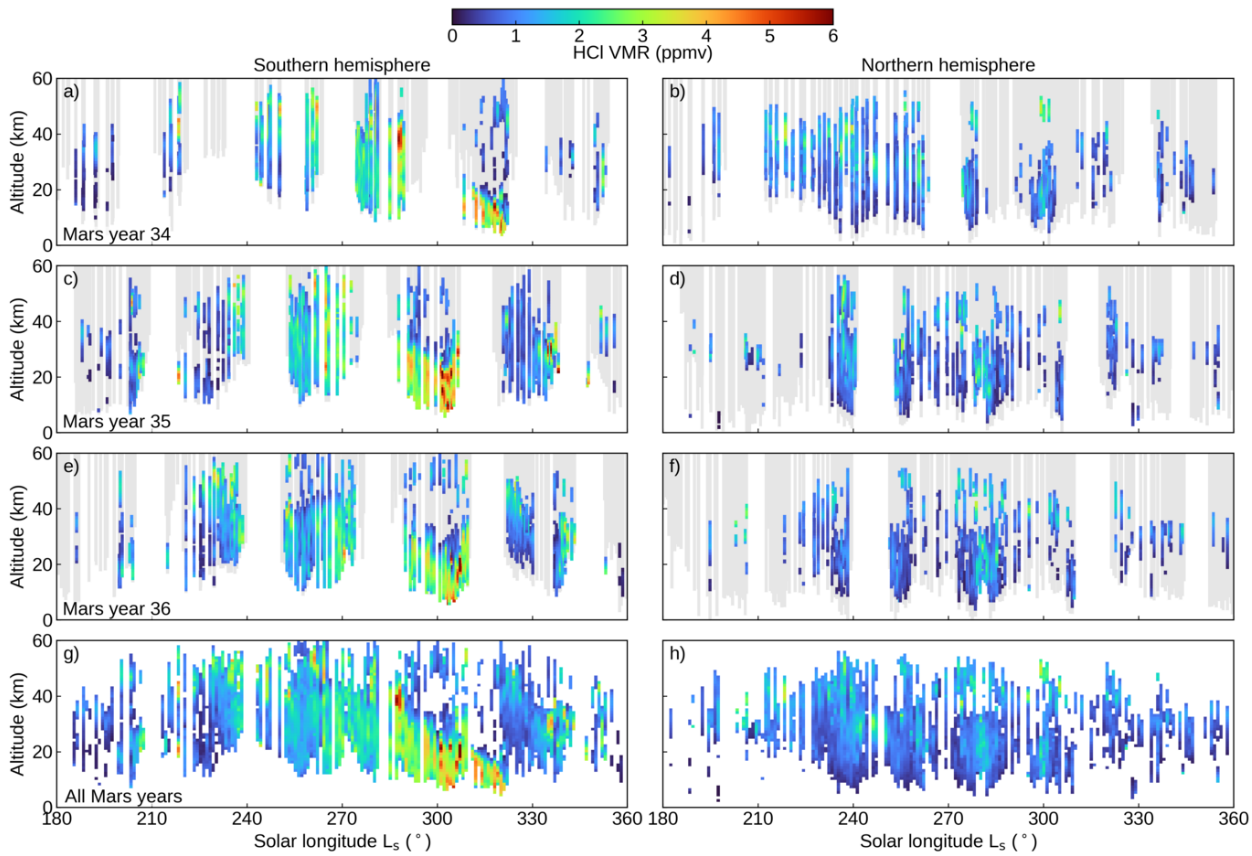

Figure 3: Climatology of HCl. The vertical profiles of HCl VMR measured using ACS MIR as a function of solar longitude (L_s). Each row of panels represents a different Mars year (MY) from 34 (a, b) to 36 (e, f). The bottom row (g, h) combines all three MYs. Columns to the left (a, c, e) show observation made in the southern hemisphere, and panels on the right (b, d, f) show observations made in the northern hemisphere. Grey shading indicates periods and altitudes where secondary grating positions 11 and 12 were used, but the VMR of HCl was below the detection threshold. The latitudes of the ACS MIR observations covered in each panel are shown in Fig. S2, which reproduces data from Fig. 1.

In the northern hemisphere, we observe a low abundance of HCl throughout the 5-50 km altitude range during most of the perihelion period. The time of its appearance is correlated with the start of seasonal dust activity (section), which leads to warmer atmospheric temperatures and an expansion of the lower atmosphere, bringing water vapour into this altitude range. VMRs observed are between 0.2 and 1.5 ppbv and remain consistent throughout the perihelion period. In MY 34, following the GDS, we see higher abundances, > 2 ppbv, between 35-45 km. These appear between L_s = 210°-240°, after which the high-altitude layer of elevated HCl VMRs falls to between 25-35 km. This layer is not seen in MYs 35 and 36, despite having had excellent coverage with ACS (see Fig. S2). This indicates that any HCl present over this period was below a detection limit of 0.2-0.5 ppbv. In these MYs we still see widespread HCl detections occurring later in the season.

HCl in the southern hemisphere is very dynamic. We are able to make sporadic detections of low abundances between L_s = 180° and 230° each year. The low number of detections in MY 34 is attributed to the GDS and its aftermath which prevented occultation measurements below 30 km for much of this period at most latitudes (Korablev et al., 2021). From L_s = 230° to 290°, we observe abundances of 2.5-3.5 ppbv at higher altitudes around 40 km. Lower abundances, on the order of 1 ppbv, are seen below.

The lower altitude limits of the observations are caused by increasing aerosol loading towards the surface. Trends are visible in the data, and this is due to the variation in latitudes of ACS MIR occultation opportunities (see Fig. 1 and S2). Closer to the gaps in coverage surrounding L_s = 250° and 280° in panels c and e of Fig. 3, the lowest altitudes available are ~ 20km. These observations correspond to low latitudes, as the occultation coverage approaches the equator. The vertical coverage extends to 5 or 10 km further from these gaps, where ACS MIR occultations are made at far southern latitudes between 60°S and 70°S.

As we approach L_s = 300° in MYs 35 and 36 (Fig. 3c and e) we see a sharp decrease in the altitude of peak HCl. VMRs at this time of year are the highest observed, between 3-5 ppbv, with the altitudes of peak abundances decreasing steadily over time. The gaps in L_s coverage are unfortunate, but combining the observation in all three MYs paints a clear picture. In MY 34 (Fig. 3a, we find a maximum abundance around 40 km at L_s = 285°. In MYs 34 and 35 (Fig. 3c and e), the peak altitude has fallen to 30 km by L_s = 290°, and continues to fall steadily to < 20 km by L_s = 305°. Returning to MY 34, this trend continues all the way until L_s = 320°, where the height of the HCl maxima is reduced to 10 km. While the latitudes of our observations change over L_s (see Fig S2) and impacts gas abundance, the overall trend described between L_s = 210-340°, occurs over mainly over a latitude band between 40°S-60°S.

This trend is ended by the onset of the annually occurring late season dust storm (often called ‘C storms’ after (Kass et al., 2016)). In MY 34, the late-season storm occurs much later than in MYs 35 and 36, around L_s = 320°, after we have seen the HCl peak-height fall to 10 km. This is shown in section and Fig. 5 using MCS data. In MYs 35 and 36, the onset of the late-season storm is around L_s = 310° to 315°, periods in which we were still making ACS MIR observations at low latitudes before the beta angle prevented occultations. At these times we see a sudden increase in the altitudes at which HCl can be detected. This is most likely due to the storm activity which is preceded by the elevation of water vapour and rapidly rising atmospheric temperatures associated with seasonal dust activity.

After the late-season dust storms, only low abundances of HCl are observed, and only at altitudes above the height of the remnants of the dust storm. Over time, the altitude range of detected HCl decreases, indicating that abundances in the upper observed altitudes is falling off. Finally, after L_s = 340°, HCl detections become sporadic again as the southern autumnal equinox approaches.

In panels g and h of Fig. 3 we have combined data from all three MYs. This is facilitated by the seasonal reproducibility of HCl and fills in the gaps in data caused by unfavourable beta angles. Panel g, for the southern hemisphere, clearly shows the overall seasonal trend in HCl behaviour, revealing its gradual change in altitude over time and the impacts of the early and late dust storms,

4.2 ACS and MCS climatologies

Using the limb observations from MCS and the solar occultations of ACS MIR, we have a clear picture of the climatological trends in the vertical distributions of several quantities that change alongside HCl, and will help explain the observed variations in HCl. In the following sections we will examine the repeating, seasonal changes in the vertical structures of dust and its impact on temperatures. These, in turn, controls the abundances of water vapour and water ice, which we will show impact to the VMR of HCl.

For example, Fig. 4 shows the vertical distribution changing over L_s for each of those quantities during southern spring and summer in MY 35. MCS data is zonally averaged between 40°S and 60°S where the majority of southern ACS MIR occultations are made in Fig. 3. The MCS dust opacity (Fig. 4a) shows a slight increase in activity around $L_s = 210°$, followed by the onset of a seasonal, regional dust storm lasting from around $L_s = 230°$ to 250°. Elevated dust levels persist through $L_s = 300°$ before visibly subsiding. At $L_s = 315°$, a second seasonal storm occurs, with a more punctuated onset. Dust is lofted above 30 km, but a decrease in opacities is seen between 5 and 20 km. The dust raised by the late-season storm falls off almost exponentially and subsides before the southern autumnal equinox.

The temperatures measured with MCS (Fig. 4b; zonally averaged) follow the vertical distribution of dust very closely. Temperatures in the upper altitudes shown in the Fig. 4 are < 175 K. Below the top of the observations of elevated dust, we observe a band that has warmed towards 200 K. Such an isotherm first rises at $L_s = 210°$ above 20 K, and then climbs above 50 km during the regional dust storm around $L_s = 230°$. It remains in place around 30 km throughout most of the perihelion period, but falling after $L_s = 300°$. It rapidly climbs again to 60 km during the late-season storm at $L_s = 315°$, falling again before the equinox.

The water ice opacity measured with MCS (Fig. 4c; zonally averaged) is generally very low at all altitudes. There is a water ice layer that corresponds to a ˜175 K isotherm throughout the season, with very low abundances above, where there is little water vapour to form ices, and below, where temperatures are too warm for the ice phase. This roughly corresponds to the hygropause height, which is a limit in the vertical extent in water vapour controlled by temperature (Liuzzi et al., 2020). The altitude level of the ice layer is clearly controlled by the atmospheric temperatures, which themselves follow the heights reached by dust.

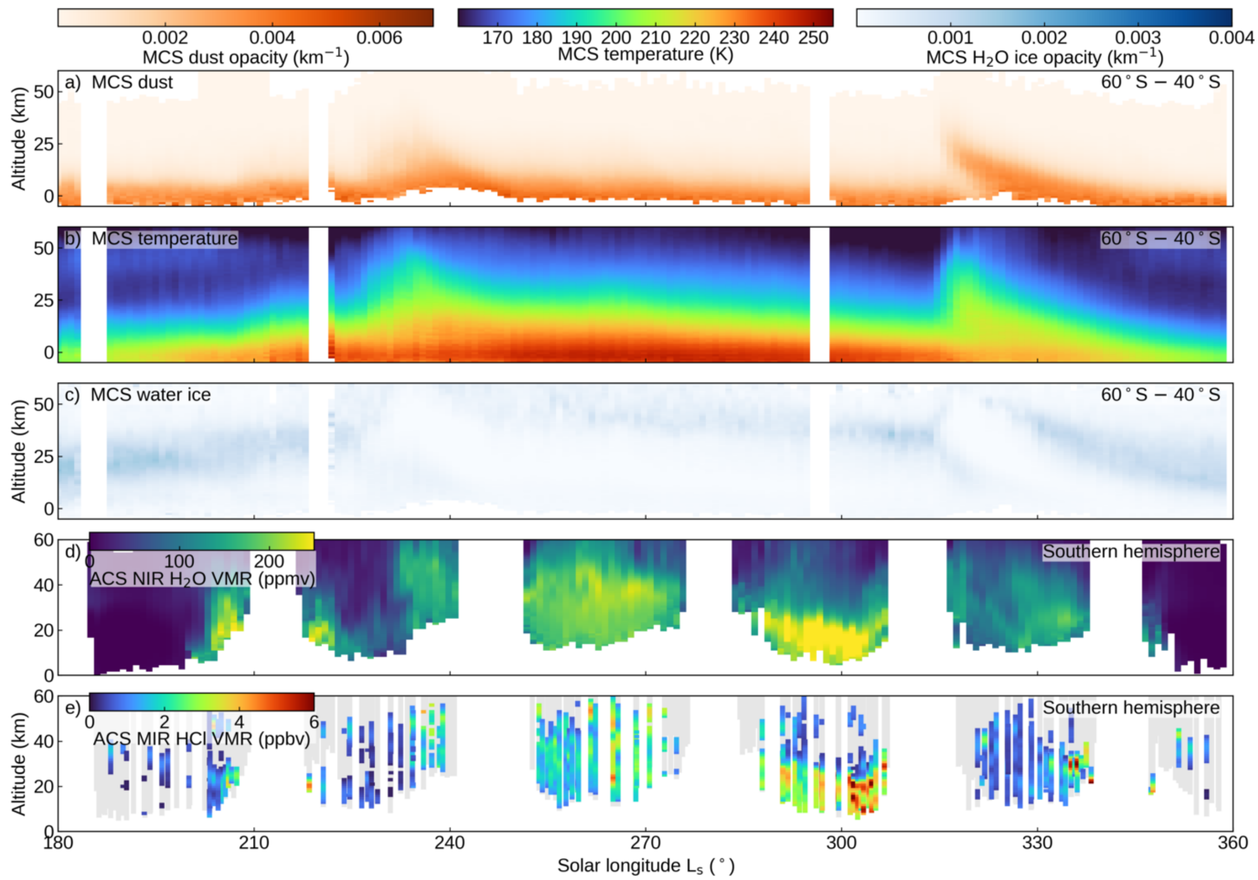

Figure 4: Example of the combined climatologies of dust, ice, temperature, H_2O, and HCl. For the southern hemisphere in MY 35, shown are: a) the dust opacity from MCS, b) temperatures from MCS, c)water ice opacity from MCS, d) water vapour VMR from ACS NIR, and e) HCl VMR from ACS MIR. The MCS data shown are zonally averaged using measurements from a mid-latitude band covering 60°S to 40°S. All altitudes are relative to the Mars areoid. The ACS data are taken at the latitudes of solar occultation tangent points shown in Fig. 1. Grey shading indicates periods and altitudes where secondary grating positions 11 and 12 were used, but the VMR of HCl was below the detection threshold.

Fig. 4d shows water vapour measured with ACS NIR. This data is restricted to the ACS tangent locations whose latitude changes over time, as shows in Fig. 1, whereas the MCS data are zonally averaged. Around L_s = 210°, we observe initial seasonal increases in water vapour from the surface to 40 km. These observations correspond to equatorial crossings in the tangent location and reflect latitudinal variations.. This is consistent with early seasonal dust lifting and atmospheric warming. After L_s = 230°, a regional dust storm has started and we observe a rapid increase in the hygropause height to above 60 km, and this remains the case through L_s = 280°, consistent with MCS observations of dust and temperature (see also (Fedorova et al., 2020) and (Fedorova et al., 2023) for a comparison of ACS NIR water vapour and temperature at the tangent locations). Between L_s = 290° and 310°, a steady decline in the vertical extent of water vapour is seen in the lead up to the late season storm, driven by cooling atmospheric temperatures following perihelion. This period features the highest concentrations of atmospheric water vapour. Following the late-season storm, we again have an elevated hygropause, but with lower concentrations than during the nominal dusty period following the regional storm at L_s = 230°. Beyond L_s = 345°, water vapour is very abruptly removed from the atmosphere at these low southern latitudes. This is due to rapid cooling and contraction of the atmosphere following the late-season storm and leading into southern fall.

Atmospheric concentrations of observed HCl, shown in Fig. 4e, closely match the behaviour of water vapour. Early observations occur at low latitudes during the equatorial crossings around $L_s = 210°$, followed by a sharp increase in vertical extent and abundance after the onset of the regional dust storm at $L_s = 230°$. Approximately 2 ppbv HCl is maintained through $L_s = 280°$ with a similar vertical limit as water vapour, which corresponds to the atmospheric temperatures and the ice condensation limit of water. After $L_s = 280°$, the vertical extent of HCl falls steadily, while its abundance grows to 3-4 ppbv. After the late-season dust storm, we make consistent HCl observations with a low abundance, but wide vertical extent, until around $L_s = 245°$, after which only sporadic observations with low confidence are made.

Versions of Fig. 4 for MYs 34 and 36 are provided in the Supplementary Information (Figs. S3 and S4). Similar figures displaying observations made over the northern hemisphere during MYs 34-36 are provided as Figs. S5-S7. This data, for each MY and hemisphere and arranged as in Fig. 3 is presented in the following sections.

4.3 Dust

In Fig. 5, we show the changes in the vertical distribution of dust measured with MCS over time. As in Fig. 4a, the MCS observations are zonally averaged over a band covering either 60°S to 40°S or 40°N to 60°N. The figure panels are divided in northern and southern hemispheres, and by Mars year.

The top panels (Fig. 5a and b) show MY 34 which was dominated by the GDS. A sharp increase in dust opacity over altitude from the surface to > 30 km can be seen between $L_s = 185$-190°. This is most pronounced in the southern hemisphere, where we see the highest opacities out of any MY. In the south, the impact of the GDS, elevated dust opacities over a wide range of altitudes, last well after $L_s = 250°$, although the planet-encircling phase of the initiating GDS event is considered to only last through $L_s = 205$-215° (Guzewich et al., 2019; Kass et al., 2019). In this main phase of the GDS, dust was lifted to above 80 km (Kass et al., 2019).

In the northern hemisphere, the initial phase of the GDS is seen as a rapid pulse in Fig. 5b, followed by several additional phases of growth and decay (see, e.g., (Guzewich et al., 2019; Kass et al., 2019)). Significantly elevated dust opacities throughout the 0-30 km altitude range relative to MYs 35 and 36 (Fig. 5d and f) are observed from $L_s = 210°$ to 270°.

MYs 35 and 36 are examples of typical Martian seasonal dust activity (Montabone et al., 2015). In the southern hemisphere (Fig. 5c and e), the average dust opacities increase after $L_s = 210°$ due to large, but regional, dust storms. This lifting phase occurs midway between the vernal equinox ($L_s = 180°$) and the perihelion point ($L_s = 251°$), and a decay phase begins between perihelion and summer solstice ($L_s = 270°$).

This is less pronounced in the northern hemisphere (Fig. 5d and f), which is characteristically absent of clear growth and decay phases. The initial dust lifting after $L_s = 220°$ is pronounced, and a clear lifting of dust to well above 30 km is observed. After this, the dust opacities remain somewhat constant through the majority of the period, with a gradual decay in the maximum vertical extent.

In all MYs, the observed dust activity is punctuated by a late season storm, seen clearly in both hemispheres. These occur between $L_s = 310$-330°, are seen to occur progressively earlier in the season from MY 34-36. These late season storms are characterized by a very sudden lifting of dust to 40-50 km, followed by a rapid decay. By $L_s = 330$-345°, dust activity is almost completely subsided, with elevated opacities restricted to < 10 km. This level and vertical extent of dust remains throughout the aphelion period (southern fall and winter) from $L_s = 0$-180°.

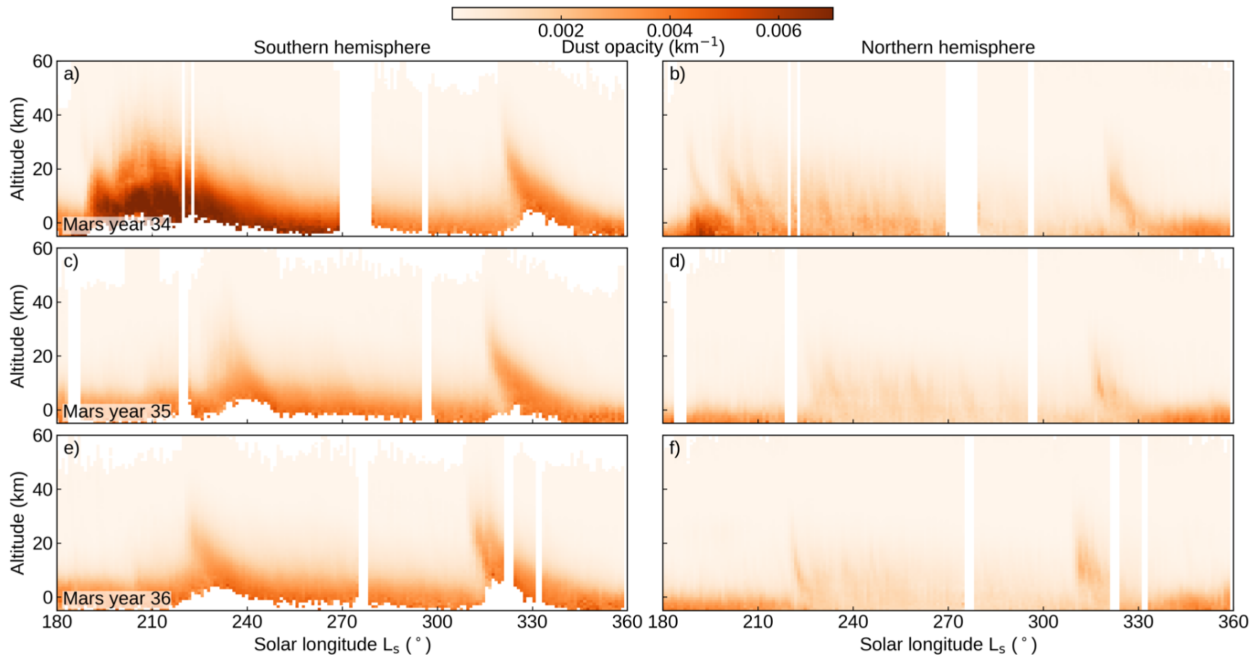

Figure 5: Climatology of dust opacity measured with MCS. The vertical profiles of dust opacity per km measured with MCS as a function of L_s. MCS data are zonally averaged over latitude bands of 40°N to 60°N for the northern hemisphere, and 60°S to 40°S for the southern hemisphere. Panel arrangements by Mars year and hemisphere are as in Fig. 3.

4.4 Temperature

When dust is lifted into the Martian atmosphere, it has a positive feedback on atmospheric temperatures by both absorbing and scattering incoming solar infrared radiation (e.g. (Pollack et al., 1979; Madeleine et al., 2011; Smith et al., 2001)). This is clearly seen in the MCS data when comparing the panels in Fig. 5, showing dust opacity, with those in Fig. 6, which show temperatures (MCS data are zonally averaged over a latitude band covering 60°S to 40°S). The zonally averaged data in Fig. 6 are lot limited by local time, as the ACS data will comprise of both morning and evening terminator observations. When zonally averaged over this L_s range, southern hemisphere MCS temperatures recorded in the afternoon/evening are significantly warmer than those at night/morning. Fig. 6 is reproduced in Figs. S8 and S9 to show the afternoon and night MCS temperature data.

Shortly after the southern vernal equinox in MY 34 (Fig. 6a and b), there is a rapid warming of the lower atmosphere that coincides with the start of the GDS. This is apparent in both the northern and southern hemisphere, and there is a visible link to the height at which dust is lifted. This is clearly visible in the vertical structure of temperatures right at the start of the GDS in which the initial phase at $L_s = 190°$ drives dust up to 25 km, which impacts atmospheric temperatures over the same altitude range. In the next phase of the GDS, after $L_s = 200°$, dust is driven well above 40 km and causes warming over the entire altitude range shown.

The dust activity during the GDS is of such severe intensity that the positive feedback mechanism between dust and temperature does not impact the entire atmosphere. At the peak of the GDS, the dust opacity grows large enough at a high enough altitude that the amount of infrared radiation reaching the lower atmosphere (below 20km) is reduced overall, limiting the amount of the warming the atmosphere experiences, and even leading to a net cooling effect above the surface (Fig. 6a and b). This is also seen in the ACS NIR temperature data (Fedorova et al., 2023).

In MYs 35 and 36, without the GDS, the warming of the atmosphere is the southern hemisphere tracks the growth of the regional dust storm activity. Increases in temperature from the surface to 10 km occur around $L_s = 210°$, but grow to cover altitudes from the surface to > 40 km when the dust opacities sharply increase at $L_s = 230°$ and 220° for MY 35 and 36, respectively. In the northern hemisphere, the impact of warming is much weaker, corresponding to the relative decrease in the dust opacity. Dust over these periods (Fig. 5d and f) exhibits a sudden lifting when the southern regional dust storms occur, which is observed as a decrease in dust opacity near the surface, and a moderate increase in opacity from the surface to well above 30 km. This lifted dust creates a warm layer in the atmosphere extending from 10 to 40 km, and lasting until the late season dust storms. Just as for the dust opacity, the upper altitude of the warm layer decays over time between $L_s = 220°$-230° and $L_s = 310°$-320°. Towards the surface, the axial tilt of Mars controls solar insolation and results in a cold layer forming that is representative of the northern fall and winter seasons.

In all three MYs shown (34-36), the late season dust storms clearly impact the vertical profiles of temperature. This is seen in all six panels of Fig. 6 as a very sudden increase in temperatures from the surface to above 50 km at some point between $L_s = 310$-330°. Just like the dust opacities following the late season storm, the upper limit of the warming decays rapidly as the southern autumnal equinox approaches.

As in Figs. 4 and 5, the temperature data measured with MCS and shown in Fig. 6 are zonally averaged over latitude bands. Vertical profiles of temperature measured with ACS NIR at the locations of TGO solar occultation opportunities over the same period (Fedorova et al., 2020; Fedorova et al., 2023), and arranged in the same manner, are shown in Fig. S10. Overall, the magnitudes and trends in temperature are consistent between MCS and ACS NIR. Differences seen in Fig. 8 are largely a result of the variability of latitude over time that is a restriction of the solar occultation technique (see Fig. S2). Quantitive validations of the temperature data products from ACS NIR and MCS are provided in (Fedorova et al., 2020) and Part II of this study (Olsen et al., 2024). A critical result that came from ACS NIR was the frequent detection of layers of the atmosphere feature water vapour supersaturation (Fedorova et al., 2020; Fedorova et al., 2023). The relationship between supersaturation and HCl is not assessed since HCl observations, restricted by the relatively low abundance of HCl and the sensitivity of ACS MIR, are only made below the hygropause, and, therefore, below where supersaturation is observed.

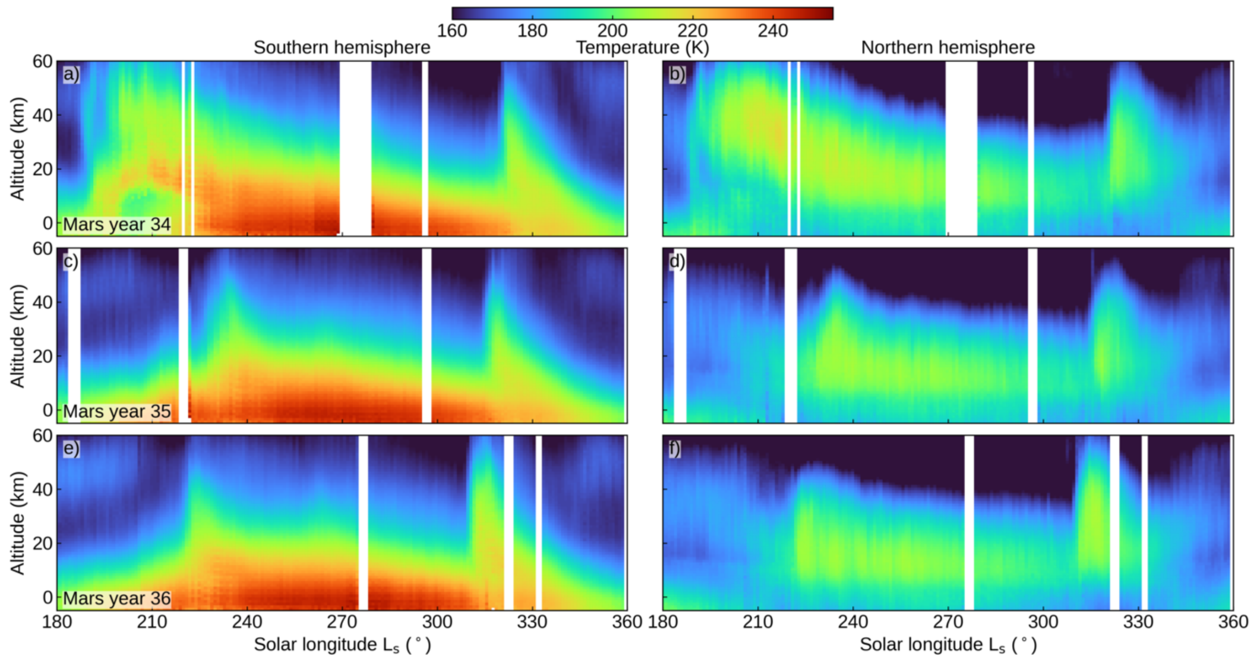

Figure 6: Climatology of temperature measured with MCS. The vertical profiles of temperature measured with MCS as a function of L_s. MCS data are zonally averaged over latitude bands of 40°N to 60°N for the northern hemisphere, and 60°S to 40°S for the southern hemisphere. Panel arrangements by Mars year and hemisphere are as in Fig. 3. Temperature measurements made using ACS NIR for the corresponding periods are shown in Fig. S10.

4.5 Water ice

The vertical distribution of water ice opacity over L_s for the southern and northern hemispheres and for MYs 34-36 are shown in Fig. 7, arranged as in Fig. 3. The MCS water ice opacities are zonally averaged over a latitude band covering 60°S to 40°S, as in Fig. 4c. In contrast to the dust opacity, the distribution of water ice over the perihelion period is characterized by a lack of ice formation throughout the lower atmosphere during the perihelion period. This is, of course, driven by the dust-induced warming over the altitude and L_s range shown.

In all six panels of Fig. 7, the sudden warming caused by intense dust activity is visible as an acute, rapid decrease in water ice. Such events include the GDS in MY 34, regional storms after $L_s = 210°$ in MYs 35 and 36, or the late season storms in each MY occurring after $L_s = 310°$. At the start of the perihelion period, the southern vernal equinox, water ice may be present, on average at most latitudes, with a band of high opacity visible at 25 km at southern latitudes, and a lower-opacity band visible at 20 km at northern latitudes. With the exception of MY 34, as spring begins in the southern hemisphere, the height of this initial water ice layer increases, while the mean opacity of water ice decreases. When the regional dust storms begin (L_s = 230° and 220° for MY 35 and 36, respectively), the signature of water ice is reduced at all altitudes almost completely. Between $L_s = 240°$ and 310°, there is evidence of the presence of water ice above 60 km, and gradually falling to 40 km, until the late season dust storms produce a second rapid warming throughout the altitude range shown. Following these dust event, elevated water ice opacity becomes visible again at 60 km, decaying very rapidly to below 20 km.

Some of the features of the southern hemisphere climate described above are also visible in the northern hemisphere. These are the impacts of the dust events, and the water ice layer present between 60 and 40 km in the period between the seasonal dust storms (L_s = 240-310°). Distinct from the southern hemisphere is the presence of water ice below 10 km. This is caused by a cold air mass close to the surface that has reduced insolation due to Mars' axial tilt. The latitude bands covered in the averaged MCS data partially cover the northern polar hood which forms during northern fall and winter and has a maximum extent between L_s = 200-320°, extending south as far as 40-45°N (Smith, 2004; Willame et al., 2017; Olsen et al., 2021; Giuranna et al., 2021).

The contours of water ice opacity shown in Fig. 7 are strongly dependent on atmospheric temperature. In comparison to Fig. 6, the location of the bands of highest water ice opacity appear to follow an isotherm of around 170-180 K (dark blue colour in Fig. 6). Close inspection will reveal that low-altitude formations in the northern hemisphere after L_s = 315° is coincident with slightly warmer atmospheric temperatures, while the high-altitude formations in the northern hemisphere occur at slightly colder temperatures. In Part II, we will show that water ice occurs over a wide temperature range (using the vertical profiles of individual measurements, rather than data that has been zonally averaged), but that ice falls off rapidly above 180 K (Olsen et al., 2024).

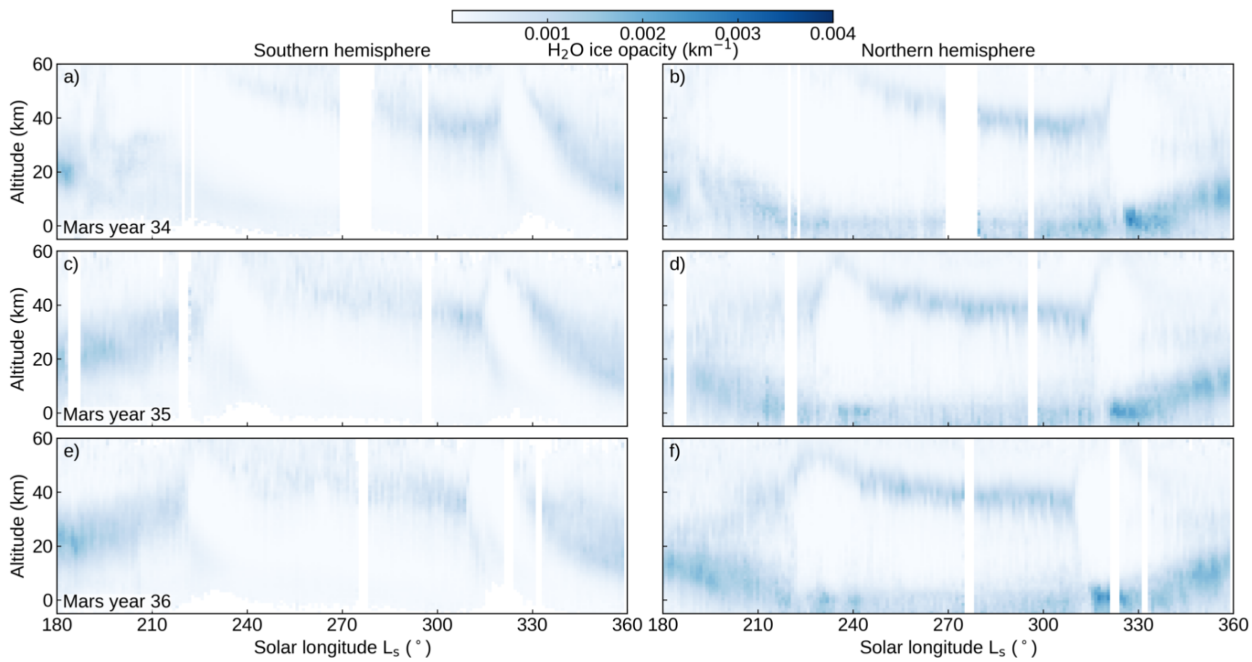

Figure 7: Climatology of water ice opacity measured with MCS. The vertical profiles of water ice opacity measured with MCS as a function of L_s. MCS data are zonally averaged over latitude bands of 40°N to 60°N for the northern hemisphere, and -60°S to 40°S for the southern hemisphere. Panel arrangements by Mars year and hemisphere are as in Fig. 3.

4.6 Water Vapour

Finally, water vapour measured with ACS NIR and ACS MIR is shown in Fig. 8. Since the ACS solar occultations are much more sparse than the MCS measurements, the data are shown for all latitudes covered with minimal averaging. The variation of latitudes over L_s corresponding to the observations shown in Fig. 8 is given in Fig. S2. Data are binned into 1° divisions of L_s and averaged. Water vapour VMR vertical profiles retrieved from ACS NIR solar occultations are only available at the time of writing through the aphelion period of MY 36 and were previously reported in (Fedorova et al., 2023). The panels in Fig. 8 corresponding to the perihelion period of MY 36 (e and f) contain water vapour VMR vertical profiles retrieved from ACS MIR. The ACS MIR observations were made using secondary grating positions 11 and 12 and are coincident with the HCl measurements shown in Fig. 3. There is good agreement between the ACS MIR and ACS NIR H_2O measurements (quantified in Part II (Olsen et al., 2024)), although the ACS MIR data is more sparse. All three MYs of ACS MIR water vapour VMR vertical profiles are shown in Fig. S1. Thorough discussions of the observations of water vapour made with ACS are provided in (Fedorova et al., 2020; Fedorova et al., 2023).

In the southern hemisphere, we observe a very dry atmosphere following the southern summer equinox, as the whole atmosphere remains impacted by the previous southern winter. In MY 34, the impact of the GDS is observed around $L_s = 190°$ as elevated VMRs between 20-60 km in both hemispheres. In MY 35, the impact of the regional dust storm is seen later in the season, corresponding to the later dust activity; with H_2O reaching lower altitudes; and with far less impact in the northern hemisphere solar occultations. Following the acute dust storms, we see elevated water vapour VMRs throughout the majority of the perihelion period. The hygropause is elevated at certain times and latitudes to well above 60 km. As we saw in the dust opacities, temperatures, and water ice opacities, the hygropause gradually decreases between $L_s = 220°$ and 320°. Unlike with the dust opacity and temperature, the decrease in the hygropause is accompanied by increasing H_2O VMRs, with the maxima reached around $L_s = 315°$ in MY 34 and between Ls = 290° and 310° in MYs 35 and 36. These maxima occur below 20 km and similar behaviour is seen in the HCl data shown in Fig. 3.

The solar occultation data reveal a strong latitudinal dependence on the impact of the late season storms. In the southern hemisphere in MY 34 (Fig. 8a), elevated water is seen reaching above 60 km, and is correspondingly visible in the northern hemisphere. These data, near $L_s = 340°$, were made at very low latitudes and are adjacent to a period of unfavourable beta angles making solar occultations impossible. Conversely, the period over which the MY 35 and 36 late season storms were observed occur at very high latitudes in both hemispheres. Elevated H_2O VMRs are observed in the southern hemisphere, where the dust intensity and temperatures are much higher, while very little water vapour is seen at the high northern latitudes beyond $L_s = 330°$.

In the northern hemisphere, over the periods between dust events, we see elevated H_2O VMRs from 10-50 km, although with lower magnitudes than in the southern hemisphere. Over this time frame ($L_s = 220°$-320°), the hygropause appears to decrease in altitude (see (Holmes et al., 2024)). This is especially apparent in MY 34, but in all MYs examined the H_2O VMR is strongly impacted by the latitudes that are varying with L_s, with larger VMRs, and corresponding higher hygropause levels, occurring at low latitudes (see Fig. S2). This overall trend is in agreement with that seen in each other variable: HCl VMR from ACS MIR; and the dust opacity, temperature, and water ice opacity from MCS.

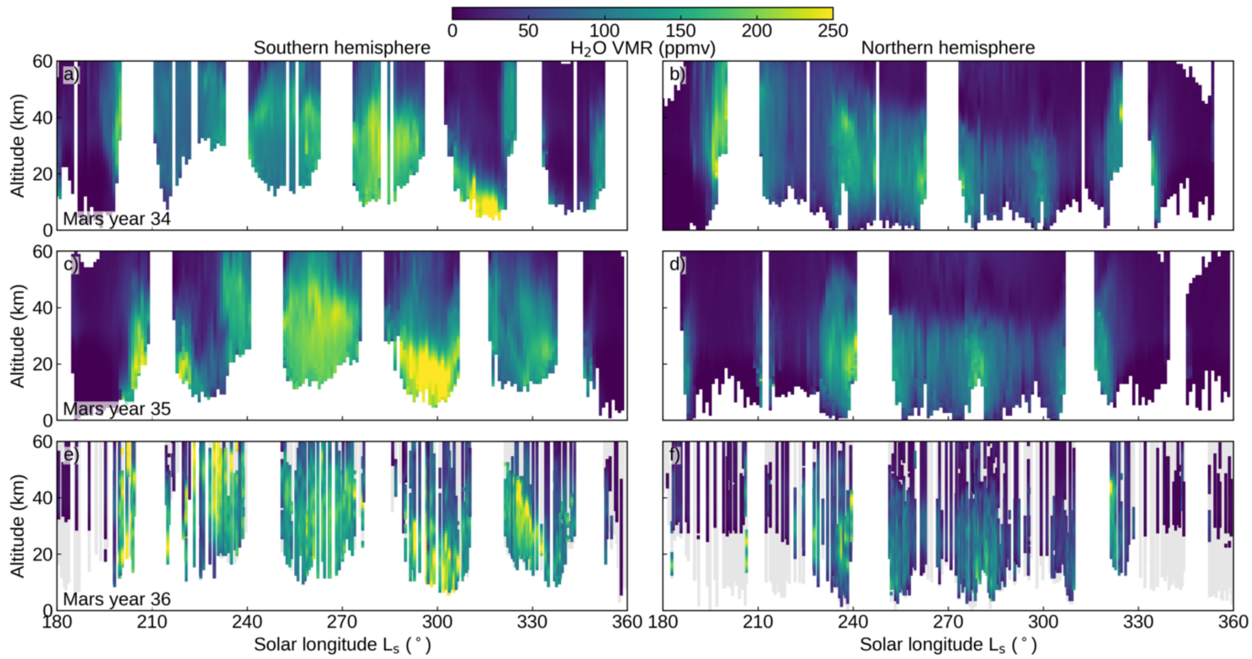

Figure 8: Climatology of water vapour measured with ACS NIR. The vertical profiles of H_2O VMR measured using ACS NIR or ACS MIR as a function of L_s. Panel arrangements by Mars year and hemisphere are as in Fig. 3. ACS NIR data is shown for MYs 34 and 35, but was not yet available over the perihelion period of MY 36. ACS MIR data is shown for MY 36. ACS MIR data for the corresponding periods over all MYs is shown in Fig. S11. The latitudes of the ACS MIR observations covered in each panel are shown in Fig. S2, which reproduces data from Fig. 1. Grey shading indicates periods and altitudes where secondary grating positions 11 and 12 were used, but the VMR of H_2O was below the detection threshold.

5 Conclusion

In every quantity examined, we observe similar seasonal trends, all linked to Mars' orbit and a cascading collection of linked physical mechanisms. Southern spring is initiated and driven two-fold: by the decreased distance between the Sun and Mars and an axial tilt that brings the sub-solar point south towards the pole. The result is a warming of the surface and atmosphere, sublimation of water and CO_2 on the southern polar cap, and increased atmospheric density and surface pressure. This leads to dust lifting and atmospheric warming. The expansion of the lower atmosphere elevates the hygropause and brings water vapour to higher altitudes.

The seasonality of the Martian atmosphere has been well observed over time, from the Earth, from nadir-pointing instruments, and from limb-viewing instruments that provide access to the vertical structure of temperature, pressure, and gas abundance. The ExoMars Trace Gas Orbiter has greatly improved our capabilities to investigate the Martian atmosphere across all scales in terms of sensitivity and coverage. This study brought together the dust and water ice aerosols opacities measured with the Mars Climate Sounder on MRO with those of the abundances of water vapour and hydrogen chloride made with the Atmospheric Chemistry Suite on TGO. The MCS data is limb-viewing, has excellent vertical resolution, and high-density data coverage. The ACS data used the solar occultation technique, has very high sensitivity to trace gas abundance and their variations along the vertical, but is much more restricted in its coverage. The seasonal evolution of temperature, dust, water ice, and water vapour have been described previously for each instrument, but this is the first comprehensive comparison of multiple measured quantities between TGO and MRO, and the first description of the seasonality of HCl, and how it compares to the other quantities.

HCl, the novel aspect of this investigation, is certainly affected dynamically and photochemically by the activities resulting from the southern spring and summer seasons. In this paper we have shown how dust lifting impacts atmospheric temperatures, which drive water vapour to higher altitudes and define the altitudes where water ice forms. The vertical extent of each parameter is linked in each Mars year observed, with the extent of dust lifting governing the heights where warming occurs, which defines the hygropause height and layer of water ice just above. Key dust events, the magnitude and timing of which is unique each year, are seen to affect all parameters consistently, with early season and late season dust storms leading to rapid increases of all parameters over a wide altitude range. At either end of the season, this is followed by a decay phase which is slow at the end of southern spring, while the atmosphere is being driven by perihelion solar insolation and optimal axial tilt, but very rapid at the end of southern summer when this is no longer the case.

HCl is shown to closely follow the behaviour of water vapour in both its vertical extent, changes over time, and even its relative abundance. This is expected behaviour for HCl since its most rapid formation mechanism should be via reaction with water vapour photolysis products. However, HCl was also expected to be a stable reservoir for atmospheric chlorine. While this study strongly suggests that the availability of water vapour controls the production rate of HCl, we do not know what the source of free Cl is for this production. While possibilities include the temporally-correlated lifted dust, or some sort of surface emission related to changes in frost cover, the rapid loss mechanisms also remain unknown. HCl is not condensible like water vapour and a change in its production mechanism at the end of the dusty season still requires a reservoir to sequester the remaining chlorine.

In Part II of this investigation, we quantify the correlations and anti-correlations between each parameter along the vertical (Olsen et al., 2024). This provides constraint to the likelihood and feasibility of each production and destruction mechanisms that we have so far considered. The paper will conclude with an in depth discussion of such mechanisms and comment on their importance and any potential issues they have.

Acknowledgements

This work was funded by the UK Space Agency (ST/T002069/1, ST/Y000196/1). The ExoMars mission is a joint mission of the European Space Agency (ESA) and Roscosmos. The ACS investigation was developed by the Laboratoire Atmosphères, Milieux, Observations Spatiales (LATMOS/CNRS) in Paris and the Space Research Institute (IKI) in Moscow. The investigation was funded by the National Centre for Space Studies of France (CNES), Roscosmos, and the Ministry of Science and Education of Russia. The GGG software suite is maintained at JPL (tccon-wiki.caltech.edu). IKI affiliates acknowledge funding from the Ministry of Science and Higher education of the Russian Federation. LATMOS affiliates acknowledge funding from CNES and ANR (PRCI, CE31 AAPG2019-MCUBE project). Open University affiliates acknowledge funding from the UK Space Agency (ST/V002295/1, ST/W00268X/1, ST/W002949/1, ST/V002295/1, ST/V005332/1, ST/X006549/1 and ST/Y000234/1. Work at the Jet Propulsion Laboratory, California Institute of Technology, was performed under contract with the National Aeronautics and Space Administration (80NM0018D0004). MCS data and assistance were provided by D.M.K. and A.K. and additional processing was performed by P.S. and J.A.H. All spectral fitting of ACS MIR data was performed by K.S.O. using the GGG software suite. Temperature and pressure data from ACS NIR were provided by A.A.F. Processing of ACS spectra is done by A.T. at IKI and by L.B. at LATMOS by L.B. Input and aid on spectral fitting, and on interpretation of data, were given by J.A., D.A.B., A.A.F., F.M., F.L., M.R.P., and J.M. Atmospheric modelling and insight into atmospheric chemistry was performed by K.R. and P.S. The ACS instrument was designed, developed, and operated by A.P., A.S., A.T., F.M., and O.K. The authors declare no conflicts of interest.

Open Research

The VMR vertical profiles generated in this study are available on the Oxford Research Archive at dx.doi.org/10.XXXX. The data sets generated by the ExoMars Trace Gas Orbiter instruments analyzed in this study are made available in the ESA Planetary Science Archive (PSA) repository, https://doi.org/10.57780/esa-rtlh14g, following a six months prior access period, and the ESA Rules on Information, Data and Intellectual Property. Temperature and pressure data used here are from ACS NIR and were generated in other studies: data from MY 34 are made available in (Fedorova et al., 2020) and an updated data version containing MYs 34-36 are published in (Fedorova et al., 2023) and can be downloaded from https://doi.org/10.17632/6xrn9v4dc5.1. Data from the MCS investigation (v5.2) are made available through the NASA Planetary Data System (PDS) and are accessible from: https://atmos.nmsu.edu/data_and_services/atmospheres_data/MARS/mcs.html. The LMD MCD v5.3 and v6.1, as well as data generated with the LMD GCM for TGO solar occultations, along with its user guide, are hosted by LMD and can be found at: http://www-mars.lmd.jussieu.fr/.

Supporting Information for

Relationships between HCl, H2O, aerosols, and temperature in the Martian atmosphere Part I: climatological outlook

K. S. Olsen[1,2], A. A. Fedorova[3], A. Kleinböhl[4], D. M. Kass[4], A. Trokhimovskiy[3], O. Korablev[3], F. Montmessin[5], F. Lefèvre[5], L. Baggio[5], J. Alday[2], D. A. Belyaev[3], J. A. Holmes[2], J. Mason[2], P. Streeter[2], K. Rajendran[2], M. R. Patel[2], A. Patrakeev[3], and A. Shakun[3+]

[1]Department of Physics, University of Oxford, Oxford, UK.

[2]School of Physical Sciences, The Open University, Milton Keynes, UK.

[3]Space Research Institute (IKI), Moscow, Russia.

[4]Jet Propulsion Laboratory, California Institute of Technology, Pasadena, USA.

[5]Laboratoire Atmospheres, Milieux, Observations Spatiales (LATMOS/CNRS), Paris, France.

Contents of this file

Figures S1 to S11

Introduction

This supporting information for **The relationship between HCl and aerosols in the Martian atmosphere I: climatological outlook** contains the supplementary figures S1 to S11. Fig. S1 shows examples of the retrieved vertical profiles of HCl and H_2O from ACS MIR; H_2O and temperature from ACS NIR; and temperature, dust opacity, and water ice opacity from MCS. Fig. S2 shows the time-varying latitudes of the ACS solar occultation measurements over the L_s and latitude ranges presented in Fig. 3. Figs. S3 and S4 are versions of Fig. 4 examining the southern hemisphere in MYs 34 and 36. Figs. S5-S7 are versions of Fig. 4 examining the northern hemisphere in MYs 34-36. Figs. S8 and S9 reproduce Fig. 6, but restrict the MCS data to mornings and evenings, respectively. Fig. S10 shows temperatures from ACS NIR arranged in the same manner as those from MCS shown in Fig. 6. Fig. S11 shows water vapour vertical profiles retrieved from ACS MIR and arranged in the same manner as those from ACS NIR in Fig. 8.

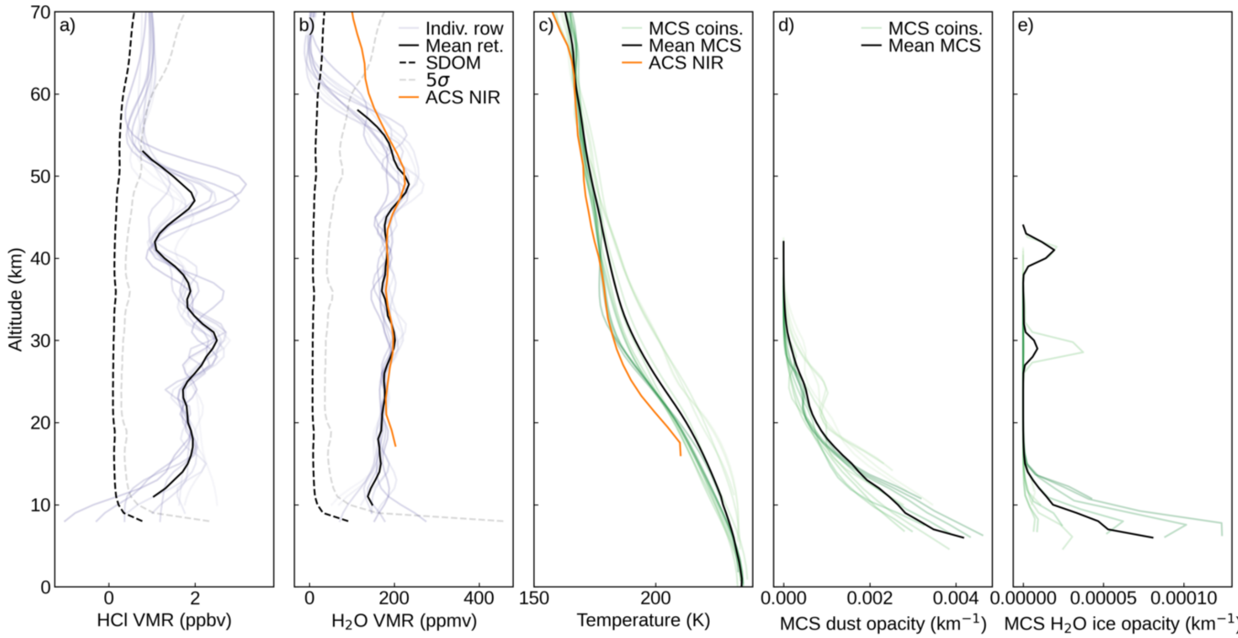

Figure S1: Example profiles from co-located measurements used in this study. The ACS MIR observation selected was number 12133_N1 and was recorded at (51.0°E,-55.7°S) on L_s = 256.75°. Panel a) shows the HCl retrieval from ACS MIR. The vertical profiles obtained for each detector row are shown in shades of purple and their weighted mean is black. The standard deviation of the mean (SDOM or σ) is dashed black, while three times the SDOM (3σ), used to define an HCl detection, is dashed grey. Panel b) shows the H_2O retrieval from ACS MIR using the same colour schemes as panel a) (but using a 5σ detection threshold). The retrieved vertical profile from a simultaneous observation made with ACS NIR is shown in orange. Panel c) shows the retrieved temperature vertical profile made using the simultaneous observation of ACS NIR (orange). Panel c) also shows the temperature retrievals from co-located MCS observations in shades of green, with their mean in black. Panel d) shows the dust opacity at 21.6 μm measured with MCS. Each co-located MCS observation is in green and their mean is in black. Panel e) shows the water ice opacity at 11.9 μm measured with MCS using the same colours as panel d).

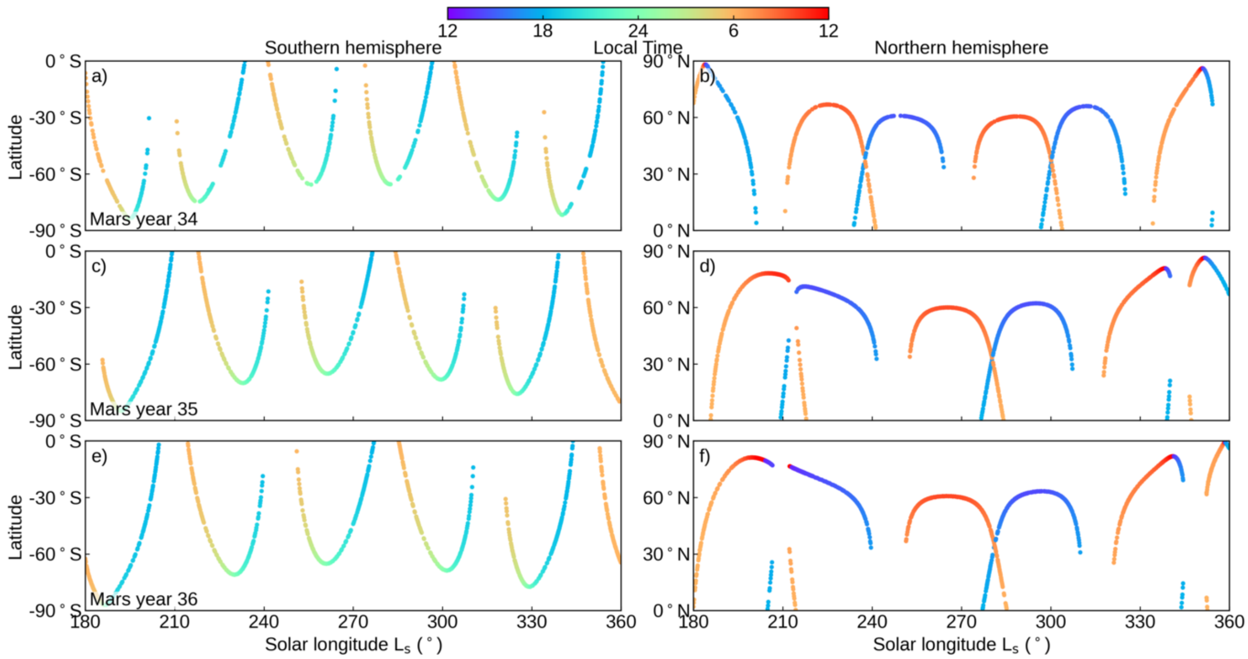

Figure S2: Distribution of the latitudes of ACS solar occultations over solar longitude (L_s). This data is a subset of that shown in Fig. 1, but arranged over the same time periods and hemispheres as Fig. 3. Colours indicate local time.

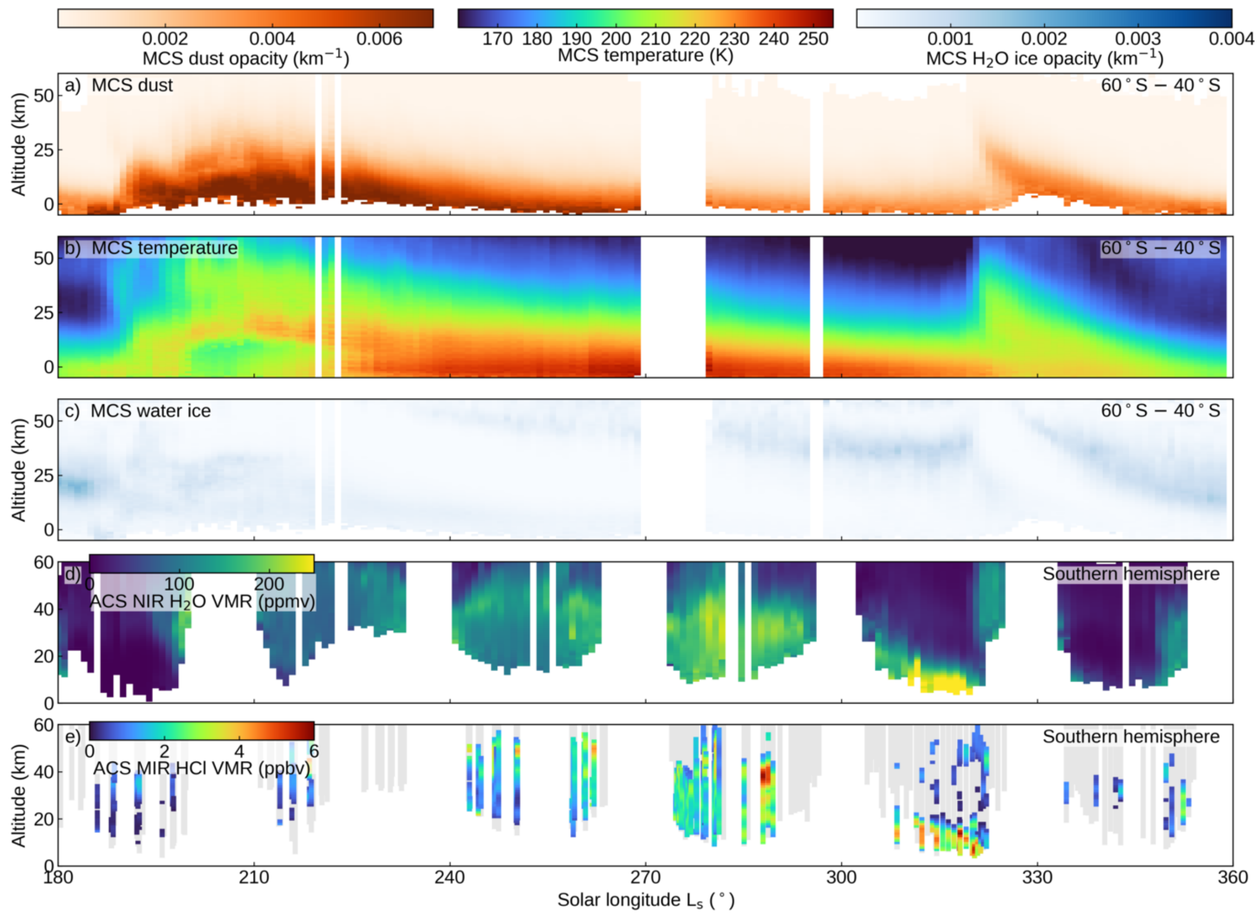

Figure S3: The combined climatologies of dust, ice, temperature, H_2O, and HCl. For the southern hemisphere in MY 34, shown are: a) the dust opacity from MCS, b) temperatures from MCS, c)water ice opacity from MCS, d) water vapour VMR from ACS NIR, and e) HCl VMR from ACS MIR. The MCS data shown are zonally averaged using measurements from a mid-latitude band covering 60°S to 40°S. The ACS data are taken at the latitudes of solar occultation tangent points shown in Fig. 1. Grey shading indicates periods and altitudes where secondary grating positions 11 and 12 were used, but the VMR of HCl (or H_2O) was below the detection threshold.

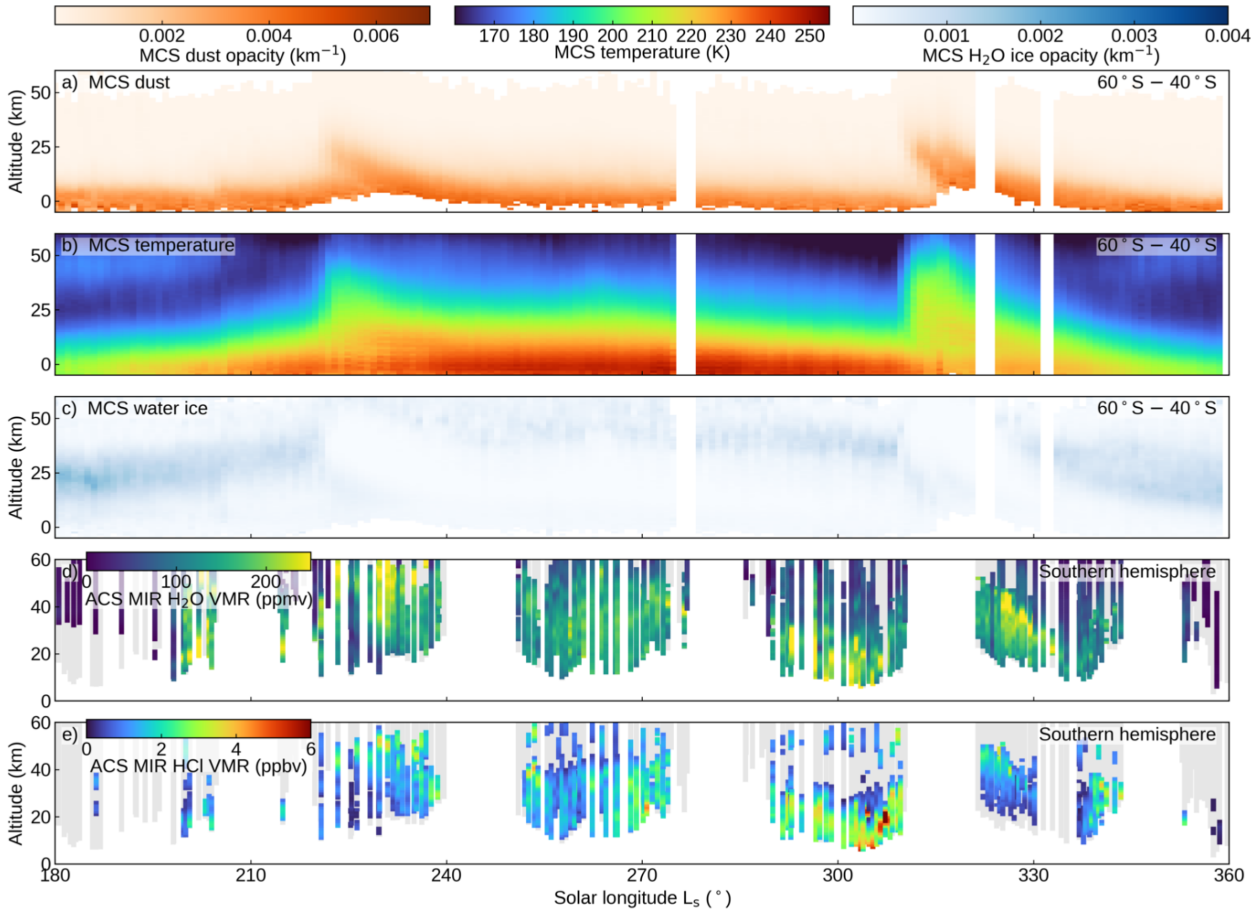

Figure S4: As in Fig. S3, but for the southern hemisphere during MY 36. Note that water vapour from ACS NIR is not available in the later half of MY 36 and panel d) features water vapour retrieved using ACS MIR spectra.

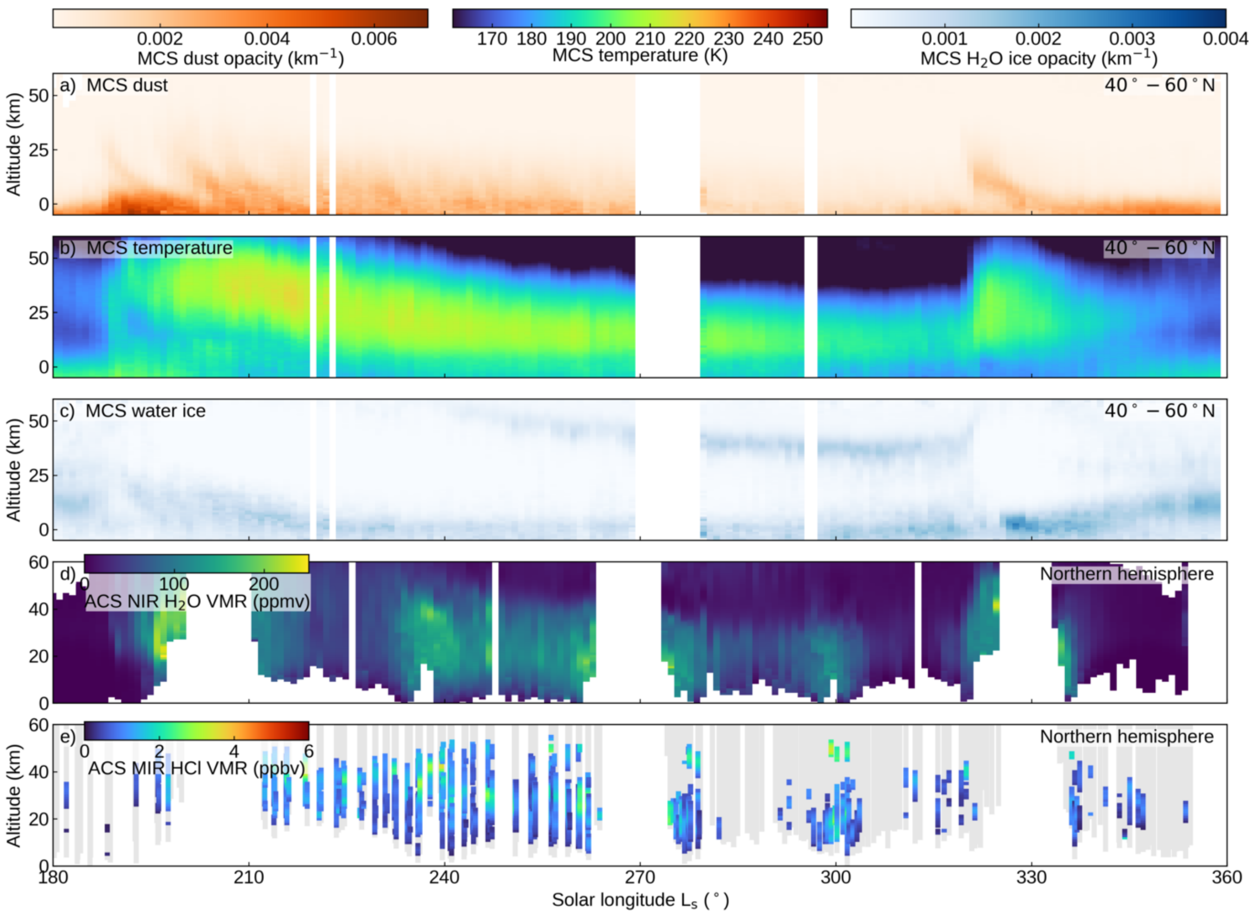

Figure S5: As in Fig. S3, but for the northern hemisphere during MY 34.

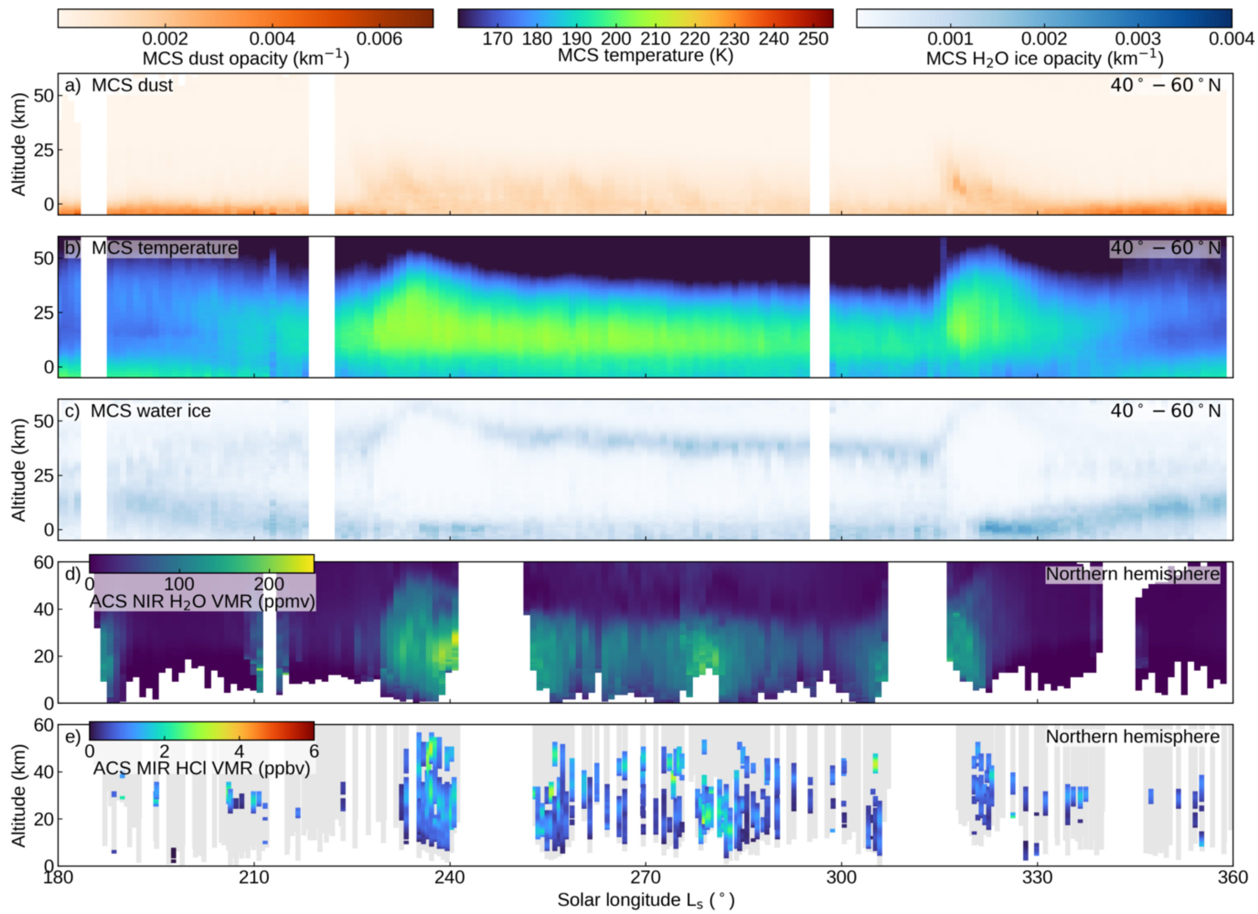

Figure S6: As in Fig. S3, but for the northern hemisphere during MY 35.

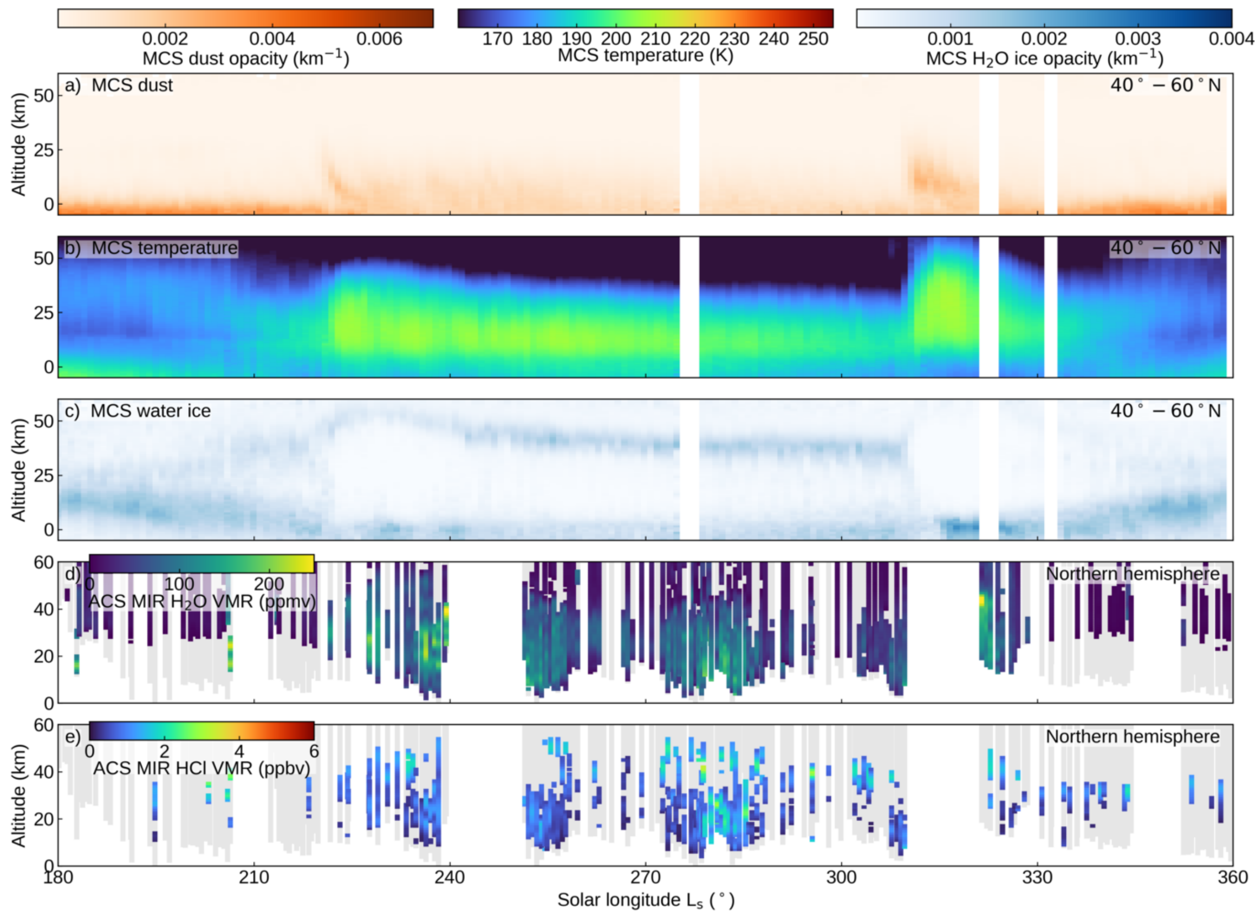

Figure S7: As in Fig. S3, but for the northern hemisphere during MY 36. Note that water vapour from ACS NIR is not available in the later half of MY 36 and panel d) features water vapour retrieved using ACS MIR spectra.

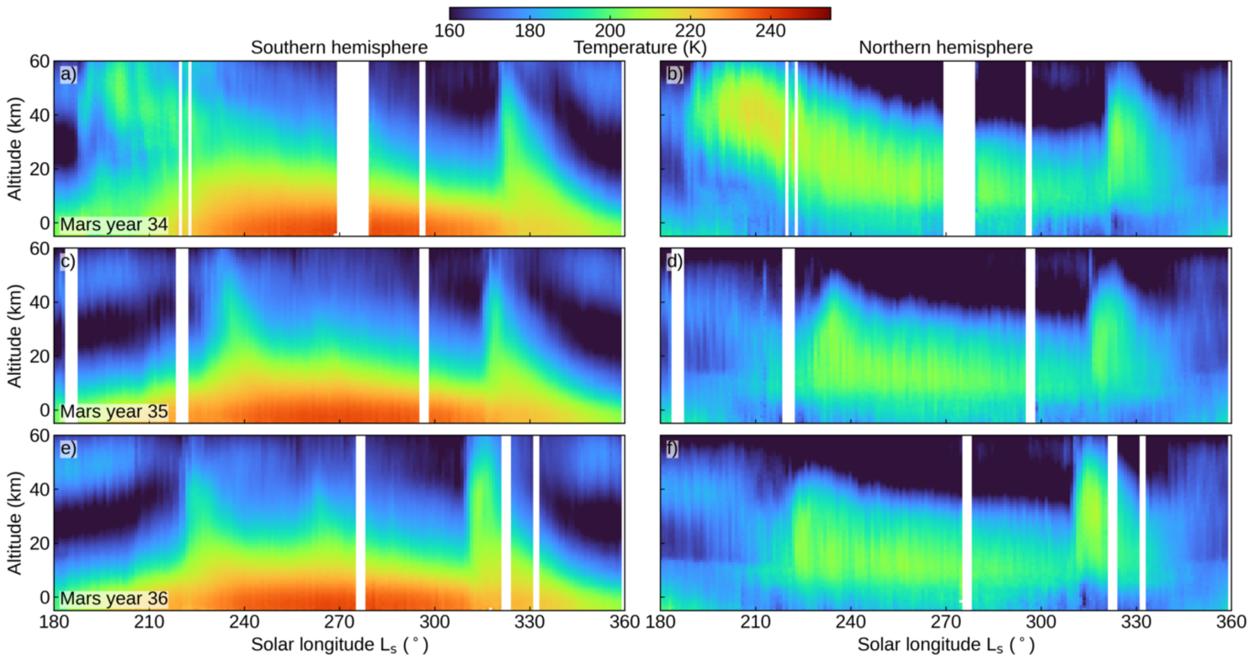

Figure S8: Climatology of temperature measured with MCS, as in Fig. 6. The vertical profiles of temperature measured with MCS as a function of L_s. MCS data are restricted to night and morning observations (local time < 12). Data are zonally averaged over latitude bands of 40°N to 60°N for the northern hemisphere, and 60°S to 40°S for the southern hemisphere. Panel arrangements by Mars year and hemisphere are as in Fig. 3.

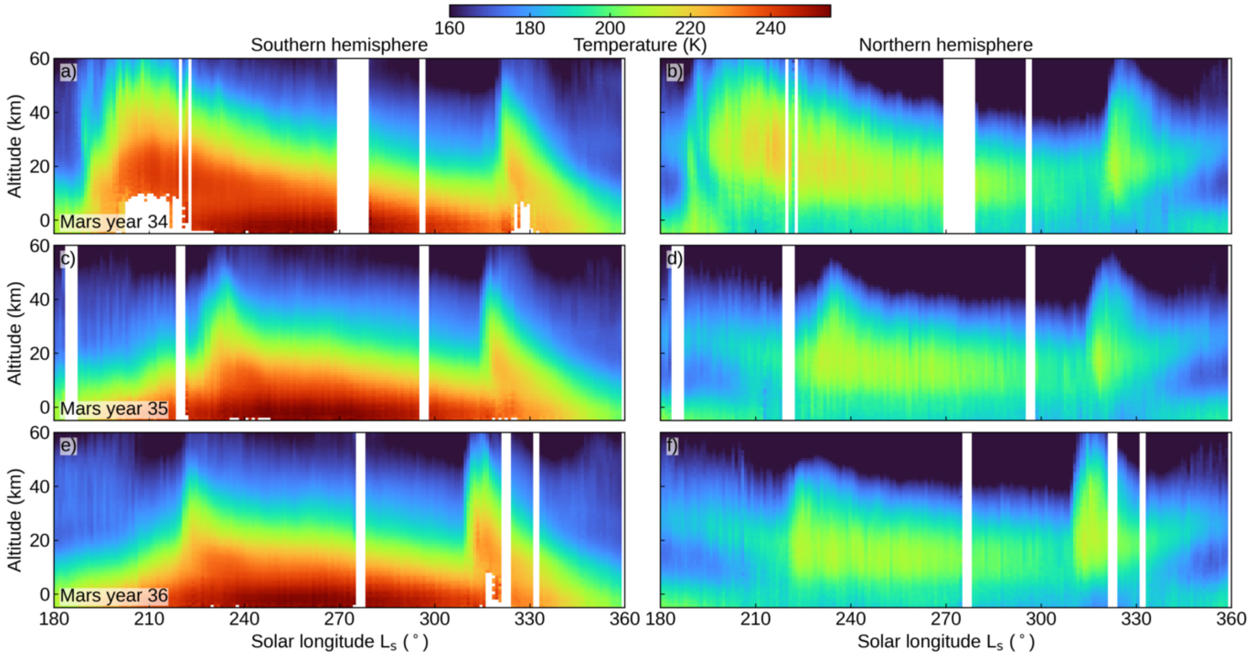

Figure S9: Climatology of temperature measured with MCS, as in Fig. 6. The vertical profiles of temperature measured with MCS as a function of L_s. MCS data are restricted to afternoon and evening observations (local time > 12). Data are zonally averaged over latitude bands of 40°N to 60°N for the northern hemisphere, and 60°S to 40°S for the southern hemisphere. Panel arrangements by Mars year and hemisphere are as in Fig. 3.

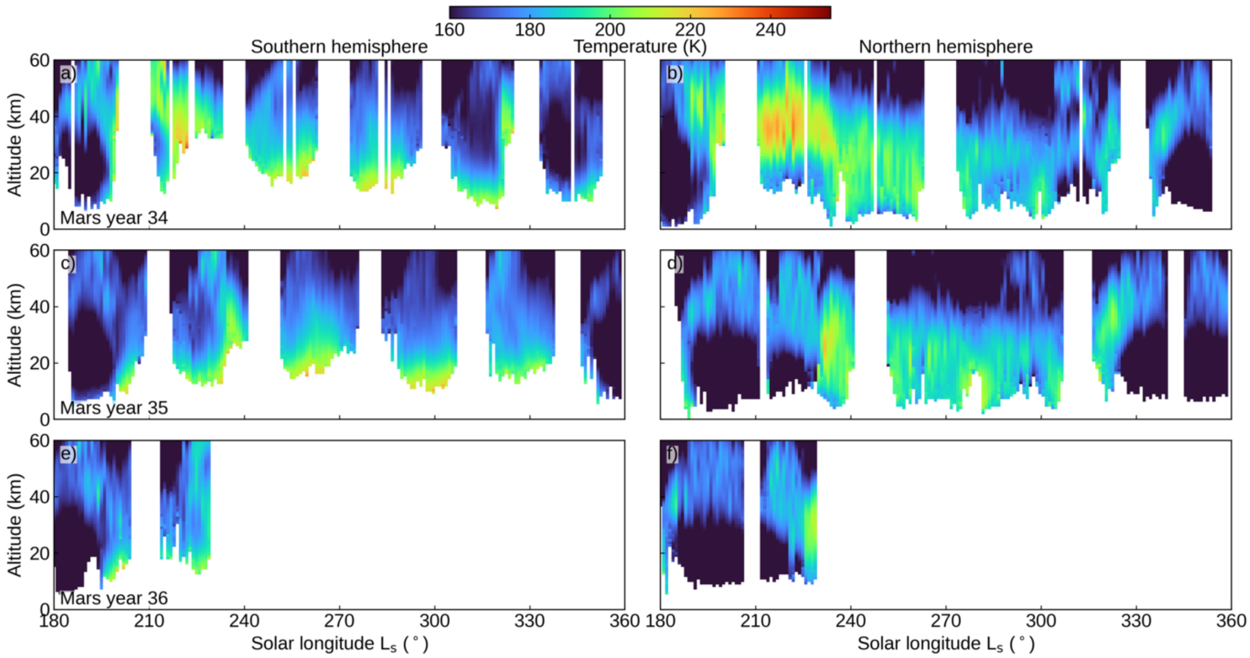

Figure S10: Climatology of Temperature. The vertical profiles of temperature measured using ACS NIR as a function of solar longitude (L_s), reproducing Fig. 6, but using ACS NIR data instead of MCS data. Arrangements of Mars year and hemisphere are as in Fig. 3. The latitudes of the ACS NIR observations covered in each panel are shown in Fig. S2, which reproduces data from Fig. 1.

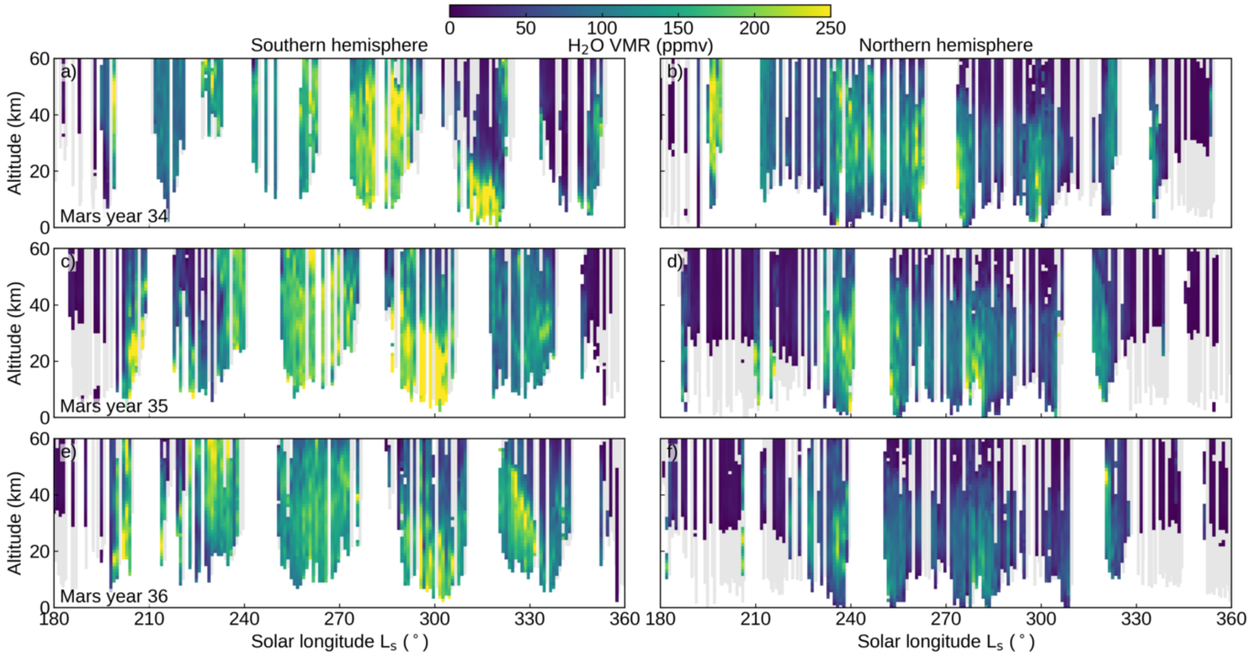

Figure S11: Climatology of water vapour. The vertical profiles of water vapour VMR measured using ACS MIR as a function of solar longitude (L_s), reproducing Fig. 8, but using ACS MIR data instead of ACS NIR data. Arrangements of Mars year and hemisphere are as in Fig. 3. Grey shading indicates periods and altitudes where secondary grating positions 11 and 12 were used, but the VMR of H_2O was below the detection threshold. The latitudes of the ACS MIR observations covered in each panel are shown in Fig. S2, which reproduces data from Fig. 1.

References

Alday, J., Trokhimovskiy, A., Patel, M. R., Fedorova, A. A., Lefèvre, F., Montmessin, F., et al. (2023). Photochemical depletion of heavy CO isotopes in the Martian atmosphere. *Nat. Astron.*. https://doi.org/10.1038/s41550-023-01974-2

Aoki, S., Daerden, F., Viscardy, S., Thomas, I. R., Erwin, J. T., Robert, S., et al. (2021). Annual Appearance of Hydrogen Chloride on Mars and a Striking Similarity With the Water Vapor Vertical Distribution Observed by TGO/NOMAD. *Geophys. Res. Lett.*, *48*(11). https://doi.org/10.1029/2021gl092506

Devi, V. M., Benner, D. C., Sung, K., Crawford, T. J., Gamache, R. R., Renaud, C. L., et al. (2017). Line parameters for CO_2- and self-broadening in the ν_3 band of $HD^{16}O$. *J. Quant. Spectrosc. Radiat. Transfer*, *203*, 158–174. https://doi.org/10.1016/j.jqsrt.2017.02.020

Fedorova, A. A., Montmessin, F., Korablev, O., Luginin, M., Trokhimovskiy, A., Belyaev, D. A., et al. (2020). Stormy water on Mars: The distribution and saturation of atmospheric water during the dusty season. *Science*, *367*(6475), 297–300. https://doi.org/10.1126/science.aay9522

Fedorova, A. A., Montmessin, F., Trokhimovskiy, A., Luginin, M., Korablev, O., Alday, J., et al. (2023). A two-Martian year survey of the water vapor saturation state on Mars based on ACS NIR/TGO occultations. *J. Geophys. Res.*, *128*(e2022JE007348), e2022JE007348. https://doi.org/10.1029/2022JE007348

Forget, F., Hourdin, F., Fournier, R., Hourdin, C., Talagrand, O., Collins, M., et al. (1999). Improved general circulation models of the Martian atmosphere from the surface to above 80 km. *J. Geophys. Res.*, *104*, 24155–24176. https://doi.org/10.1029/1999JE001025

Gamache, R. R., Farese, M., & Renaud, C. L. (2016). A spectral line list for water isotopologues in the 1100-4100 $cm^{-1\$}$ region for application to CO_2-rich planetary atmospheres. *J. Mol. Spectrosc.*, *326*, 144–150. https://doi.org/10.1016/j.jms.2015.09.001

Giuranna, M., Wolkenberg, P., Grassi, D., Aronica, A., Aoki, S., Scaccabarozzi, D., et al. (2021). The current weather and climate of Mars: 12years of atmospheric monitoring by the Planetary Fourier Spectrometer on Mars Express. *Icarus*, *353*. https://doi.org/10.1016/j.icarus.2019.113406

Gordon, I. E., Rothman, L. S., Hargreaves, R. J., Hashemi, R., Karlovets, E. V., Skinner, F. M., et al. (2021). The HITRAN2020 molecular spectroscopic database. *J. Quant. Spectrosc. Radiat. Transf.*, 107949. https://doi.org/10.1016/j.jqsrt.2021.107949

Graedel, T. E., & Keene, W. C. (1995). Tropospheric budget of reactive chlorine. *Global Biogeochemical Cycles*, *9*(1). https://doi.org/10.1029/94gb03103

Guzewich, S. D., Lemmon, M., Smith, C. L., Martínez, G., Vicente-Retortillo, Á. de, Newman, C. E., et al. (2019). Mars Science Laboratory Observations of the 2018/Mars Year 34 Global Dust Storm. *Geophysical Research Letters*, *46*(1), 71–79. https://doi.org/10.1029/2018GL080839

Hartogh, P., Jarchow, C., Lellouch, E., Val-Borro, M. de, Rengel, M., Moreno, R., et al. (2010). Herschel/HIFI observations of Mars: First detection of O_2 at submillimetre wavelengths and upper limits on HCl and H_2O_2. *Astron. Astrophys.*, *521*, L49. https://doi.org/10.1051/0004-6361/201015160

Holmes, J. A., Lewis, S. R., Patel, M. R., J. Alday, J., Olsen, K. S., Aoki, S., et al. (2024). Global mapping of the martian hygropause: links to atmospheric dust and water loss. *Geophys. Res. Lett.*, *51*.

Irion, F. W., Gunson, M. R., Toon, G. C., Chang, A. Y., Eldering, A., Mahieu, E., et al. (2002). Atmospheric Trace Molecule Spectroscopy (ATMOS) Experiment Version 3 data retrievals. *Appl. Opt.*, *41*, 6968–6979. https://doi.org/10.1364/AO.41.006968

Kass, D. M., Kleinböhl, A., McCleese, D. J., Schofield, J. T., & Smith, M. D. (2016). Interannual similarity in the Martian atmosphere during the dust storm season. *Geophys. Res. Lett.*, *43*(12), 6111–6118. https:

//doi.org/10.1002/2016gl068978

Kass, D. M., Schofield, J. T., Kleinböhl, A., McCleese, D. J., Heavens, N. G., Shirley, J. H., & Steele, L. J. (2019). Mars Climate Sounder observation of Mars' 2018 global dust storm. *J. Geophys. Res.*, *47*(23), e2019GL083931. https://doi.org/10.1029/2019GL083931

Keene, W. C., Khalil, M. A. K., Erickson, D. J., McCulloch, A., Graedel, T. E., Lobert, J. M., et al. (1999). Composite global emissions of reactive chlorine from anthropogenic and natural sources: Reactive Chlorine Emissions Inventory. *J. Geophys. Res.*, *104*(D7). https://doi.org/10.1029/1998jd100084

Kleinböhl, A., Friedson, A. J., & Schofield, J. T. (2017). Two-dimensional radiative transfer for the retrieval of limb emission measurements in the martian atmosphere. *J. Quant. Spectrosc. Radiat. Transfer.*, *187*, 511–522. https://doi.org/10.1016/j.jqsrt.2016.07.009

Kleinböhl, A., Schofield, J. T., Kass, D. M., Abdou, W. A., Backus, C. R., Sen, B., et al. (2009). Mars Climate Sounder limb profile retrieval of atmospheric temperature, pressure, and dust and water ice opacity. *J. Geophys. Res.*, *114*(E13), E10006. https://doi.org/10.1029/2009JE003358

Kleinböhl, A., Spiga, A., Kass, D. M., J, H. S., Millour, E., Montabone, L., & Forget, F. (2020). Diurnal Variations of Dust During the 2018 Global Dust Storm Observed by the Mars Climate Sounder. *J. Geophys. Res.*, *125*(1), e2019JE006115. https://doi.org/10.1029/2019je006115

Korablev, O., Montmessin, F., Trokhimovskiy, A., Fedorova, A. A., Shakun, A. V., Grigoriev, A. V., et al. (2018). The Atmospheric Chemistry Suite (ACS) of Three Spectrometers for the ExoMars 2016 Trace Gas Orbiter. *Space Sci. Rev.*, *214*(1), 7. https://doi.org/10.1007/s11214-017-0437-6

Krasnopolsky, V. A., Bjoraker, G. L., Mumma, M. J., & Jennings, D. E. (1997). High-resolution spectroscopy of Mars at 3.7 and 8 µm: A sensitive search for H_2O_2, H_2CO, HCl, and CH_4, and detection of HDO. *J. Geophys. Res.*, *102*(E3). https://doi.org/10.1029/96je03766

Lefèvre, F., Trokhimovskiy, A., Fedorova, A., Baggio, L., Lacombe, G., Määttänen, A., et al. (2021). Relationship Between the Ozone and Water Vapor Columns on Mars as Observed by SPICAM and Calculated by a Global Climate Model. *J. Geophys. Res.*, *126*(4), e2021JE006838. https://doi.org/10.1029/2021JE006838

Liuzzi, G., Villanueva, G. L., Crismani, M. M. J., Smith, M. D., Mumma, M. J., Daerden, F., et al. (2020). Strong Variability of Martian Water Ice Clouds During Dust Storms Revealed From ExoMars Trace Gas Orbiter/NOMAD. *J. Geophys. Res.*, *125*(4). https://doi.org/10.1029/2019je006250

Liuzzi, G., Villanueva, G. L., Viscardy, S., Mège, D., Crismani, M. M. J., Aoki, S., et al. (2021). Probing the Atmospheric Cl Isotopic Ratio on Mars: Implications for Planetary Evolution and Atmospheric Chemistry. *Geophys. Res. Lett.*, *48*(9). https://doi.org/10.1029/2021gl092650

Madeleine, J.-B., Forget, F., Millour, E., Montabone, L., & Wolff, M. J. (2011). Revisiting the radiative impact of dust on Mars using the LMD Global Climate Model. *J. Geophys. Res.*, *116*(E15), E11010.

McCleese, D. J., Schofield, J. T., Taylor, F. W., Calcutt, S. B., Foote, M. C., Kass, D. M., et al. (2007). Mars Climate Sounder: An investigation of thermal and water vapor structure dust and condensate distributions in the atmosphere, and energy balance of the polar regions. *J. Geophys. Res.*, *112*(E5), E05S06. https://doi.org/10.1029/2006je002790

Montabone, L., Forget, F., Millour, E., Wilson, R. J., Lewis, S. R., Cantor, B., et al. (2015). Eight-year climatology of dust optical depth on Mars. *Icarus*, *251*, 65–95. https://doi.org/10.1016/j.icarus.2014.12.034

Montabone, L., Spiga, A., Kass, D. M., Kleinb ohl, A., Forget, F., & Millour, E. (2020). Martian Year 34 Column Dust Climatology from Mars Climate Sounder Observations: Reconstructed Maps and Model Simulations. *J. Geophys. Res.*, *125*(8), e2019JE006111. https://doi.org/10.1029/2019je006111

Olsen, K. S., Fedorova, A. A., Kass, D. M., Kleinböhl, A., Trokhimovskiy, A., Korablev, O. I., et al. (2024). Relationships between HCl, H2O, aerosols, and temperature in the Martian atmosphere Part II: quantitative correlations. *J. Geophys. Res.*, *129*.

Olsen, K. S., Fedorova, A. A., Trokhimovskiy, A., Montmessin, F., Lefèvre, F., Korablev, O., et al. (2022). Seasonal Changes in the Vertical Structure of Ozone in the Martian Lower Atmosphere and Its Relationship to Water Vapor. *J. Geoph. Res.*, *127*(10), e2022JE007213. https://doi.org/10.1029/2022je007213

Olsen, K. S., Forget, F., Madeleine, J.-B., Szantai, A., Audouard, J., Geminale, A., et al. (2021). Retrieval of the water ice column and physical properties of water-ice clouds in the martian atmosphere using the OMEGA imaging spectrometer. *Icarus*, *353*, 113229. https://doi.org/10.1016/j.icarus.2019.03.006

Olsen, K. S., Lefèvre, F., Montmessin, F., Trokhimovskiy, A., Baggio, L., Fedorova, A., et al. (2020). First detection of ozone in the mid-infrared at Mars: implications for methane detection. *Astron. Astrophys.*, *639*, A141. https://doi.org/10.1051/0004-6361/202038125

Olsen, K. S., Lefèvre, F., Montmessin, F., Fedorova, A. A., Trokhimovskiy, A., Baggio, L., et al. (2021). The vertical structure of CO in the Martian atmosphere from the ExoMars Trace Gas Orbiter. *Nat. Geosci.*, *14*(2), 67–71. https://doi.org/10.1038/s41561-020-00678-w

Olsen, K. S., Trokhimovskiy, A., Montabone, L., Fedorova, A. A., Luginin, M., Lefèvre, F., et al. (2021). Seasonal reappearance of HCl in the atmosphere of Mars during the Mars year 35 dusty season. *Astronomy & Astrophysics*, *647*, A161. https://doi.org/10.1051/0004-6361/202140329

Pollack, J. B., Colburn, D. S., Flasar, F. M., Kahn, R., Carlston, C. E., & Pidek, D. (1979). Properties and effects of dust particles suspended in the Martian atmosphere. *J.Geophys. Res.*, *84*(B6). https://doi.org/10.1029/jb084ib06p02929

Sen, B., Toon, G. C., Blavier, J.-F., Fleming, E. L., & Jackman, C. H. (1996). Balloon-borne observations of midlatitude fluorine abundance. *J. Geophys. Res.*, *101*, 9045–9054. https://doi.org/10.1029/96JD00227

Smith, M. D. (2019). THEMIS Observations of the 2018 Mars Global Dust Storm. *J. Geophys. Res.*, *124*(11), 2929–2944. https://doi.org/10.1029/2019JE006107

Smith, M. D. (2004). Interannual variability in TES atmospheric observations of Mars during 1999-2003. *Icarus*, *167*, 148–165. https://doi.org/10.1016/j.icarus.2003.09.010

Smith, M. D., Pearl, J. C., Conrath, B. J., & Christensen, P. R. (2001). One Martian year of atmospheric observations by the thermal emission spectrometer. *Geophys, Res. Lett.*, *28*(22). https://doi.org/10.1029/2001gl013608

Trokhimovskiy, A., Fedorova, A. A., Olsen, K. S., Alday, J., Korablev, O., Montmessin, F., et al. (2021). Isotopes of chlorine from HCl in the Martian atmosphere. *Astron. Astrophys.*, *651*. https://doi.org/10.1051/0004-6361/202140916

Trokhimovskiy, A., Perevalov, V., Korablev, O., Fedorova, A. F., Olsen, K. .S., Bertaux, J.-L., et al. (2020). First observation of the magnetic dipole CO main isotopologue absorption band at 3.3 µm in the atmosphere of Mars by ACS. *Astron. Astrophys.*, *639*, A142. https://doi.org/10.1051/0004-6361/202038134

Villanueva, G. L., Mumma, M. J., Novak, R. E., Radeva, Y. L., Käufl, H. U., Smette, A., et al. (2013). A sensitive search for organics (CH_4, CH_3OH, H_2CO, C_2H_6, C_2H_2, C_2H_4), hydroperoxyl (HO_2), nitrogen compounds (N_2O, NH_3, HCN) and chlorine species (HCl, CH_3Cl) on Mars using ground-based high-resolution infrared spectroscopy. *Icarus*, *223*, 11–27. https://doi.org/10.1016/j.icarus.2012.11.013

Wang, X., Jacob, D. J., Eastham, S. D., Sulprizio, M. P., Zhu, L., Chen, Q., et al. (2019). The role of chlorine in global tropospheric chemistry. *Atmos. Chem. Phys.*, *19*(6). https://doi.org/10.5194/acp-19-3981-2019

Willame, Y., Vandaele, A. C., Depiesse, C., Lefèvre, F., Letocart, V., Gillotay, D., & Montmessin, F. (2017). Retrieving cloud, dust and ozone abundances in the Martian atmosphere using SPICAM/UV nadir spectra. *Planet. Space Sci.*, *142*, 9–25. https://doi.org/10.1016/j.pss.2017.04.011

Wilzewski, J. S., Gordon, I. E., Kochanov, R. V., Hill, C., & Rothman, L. S. (2016). H_2, He, and CO_2 line-broadening coefficients, pressure shifts and temperature-dependence exponents for the HITRAN database. Part 1: SO_2, NH_3, HF, HCl, OCS and C_2H_2. *J. Quant. Spectrosc. Radiat. Transfer*, *168*, 193–206. https://doi.org/10.1016/j.jqsrt.2015.09.003

Wong, A.-S., Atreya, S. K., & E., T. (2003). Chemical markers of possible hot spots on Mars. *J. Geophys. Res.*, *108*(E4), 5026. https://doi.org/10.1029/2002JE002003

Wunch, D., Toon, G. C., Blavier, J. L., Washenfelder, R. A., Notholt, J., Connor, B. J., et al. (2011). The Total Carbon Column Observing Network. *Phil. Trans. R. Soc. A*, *369*, 2087–2112. https://doi.org/10.1098/rsta.2010.0240

Zurek, R. W., & Smrekar, S. E. (2007). An overview of the Mars Reconnaissance Orbiter (MRO) science mission. *J. Of Geophys. Res.*, *112*(E5). https://doi.org/10.1029/2006je002701

Glasow, R. von, & Crutzen, P. J. (2003). Tropospheric Halogen Chemistry. In *Treatise on Geochemistry* (pp. 1–67). Elsevier. https://doi.org/10.1016/b0-08-043751-6/04141-4

Korablev, O., Olsen, K. S., Trokhimovskiy, A., Lefèvre, F., Montmessin, F., Fedorova, A. A., et al. (2021). Transient HCl in the atmosphere of Mars. *Sci. Adv.*, *7*(7), eabe4386. https://doi.org/10.1126/sciadv.abe4386